Baerenzung, J., Holschneider, M., Lesur, V. (2014): Bayesian inversion of the filtered flow at the earth's core mantle boundary. - *Journal of Geophysical Research*, *119*, 4, p. 2695-2720

DOI: http://doi.org/10.1002/2013JB010358

AGU PUBLICATIONS

JGR

Journal of Geophysical Research: Solid Earth

RESEARCH ARTICLE

10.1002/2013JB010358

Bayesian inversion for the filtered flow at the Earth's core-mantle boundary

Julien Baerenzung[1], Matthias Holschneider[1], and Vincent Lesur[2]

[1]Institute for Mathematics, University of Potsdam, Potsdam, Germany, [2]Helmholtz Center Potsdam, GFZ German Research Centre for Geosciences, Potsdam, Germany

Key Points:
- Derivation of a large-scale induction equation
- Study of the full velocity field posterior

Correspondence to:
J. Baerenzung,
baeren@voila.fr

Citation:
Baerenzung, J., M. Holschneider, and V. Lesur (2014), Bayesian inversion for the filtered flow at the Earth's core-mantle boundary, *J. Geophys. Res. Solid Earth*, *119*, 2695–2720, doi:10.1002/2013JB010358.

Received 28 MAY 2013
Accepted 4 MAR 2014
Accepted article online 11 MAR 2014
Published online 29 APR 2014

Abstract The inverse problem of determining the flow at the Earth's core-mantle boundary according to an outer core magnetic field and secular variation model has been investigated through a Bayesian formalism. To circumvent the issue arising from the truncated nature of the available fields, we combined two modeling methods. In the first step, we applied a filter on the magnetic field to isolate its large scales by reducing the energy contained in its small scales, we then derived the dynamical equation, referred as filtered frozen flux equation, describing the spatiotemporal evolution of the filtered part of the field. In the second step, we proposed a statistical parametrization of the filtered magnetic field in order to account for both its remaining unresolved scales and its large-scale uncertainties. These two modeling techniques were then included in the Bayesian formulation of the inverse problem. To explore the complex posterior distribution of the velocity field resulting from this development, we numerically implemented an algorithm based on Markov chain Monte Carlo methods. After evaluating our approach on synthetic data and comparing it to previously introduced methods, we applied it to a magnetic field model derived from satellite data for the single epoch 2005.0. We could confirm the existence of specific features already observed in previous studies. In particular, we retrieved the planetary scale eccentric gyre characteristic of flow evaluated under the compressible quasi-geostrophy assumption although this hypothesis was not considered in our study. In addition, through the sampling of the velocity field posterior distribution, we could evaluate the reliability, at any spatial location and at any scale, of the flow we calculated. The flow uncertainties we determined are nevertheless conditioned by the choice of the prior constraints we applied to the velocity field.

1. Introduction

The core magnetic field (MF) of the Earth is sustained by the dynamo action taking place in its outer core. Here the variations in chemical composition and in temperature of the liquid metal allow convection to develop. Since the fluid is electrically conducting, it interacts nonlinearly with the magnetic field. While the flow is advecting the MF, this latter is constraining the fluid motions through the Lorentz forces. The evolution of the fluid velocity field (VF) and the magnetic field are therefore entirely connected to one another through energy exchanges between them.

Studying such a system is difficult in many aspects. From a numerical point of view, simulating directly the dynamic of the outer core is a challenging task. Because of the strong regime of turbulence that the magnetohydrodynamic (MHD) flow exhibits, the separation between the smallest and the largest scales of the system is extremely broad. Yet to properly describe the evolution of both the VF and the MF, all these scales should be considered in simulations since they interact nonlinearly together. However, this is, with the actual computation power available, impossible.

From an observational point of view, direct observation of the evolution of the outer core is also impossible. Nevertheless, measurements of the MF from ground observatories or satellites may allow to indirectly infer some dynamical properties of the flow and the MF in the core. In particular, because of the low conductivity of the mantle [*Velímský*, 2010], a knowledge of the core MF at the Earth's surface is sufficient to evaluate it at the level of the core-mantle boundary (CMB). At this very specific location, the MF is coupled to the outer core VF through the frozen flux equation (a simplified version of the induction equation introduced by *Roberts and Scott* [1965], and in which the diffusion effects are neglected). By inverting this equation, it is therefore possible to evaluate the VF at the CMB. Unfortunately, the problem is ill posed for different

reasons. First, the two components of the velocity field are connected to the radial component of the secular variation (SV) through a unique equation. Then, the available secular variation given by MF models such as the second generation of the GFZ Reference Internal Magnetic Model (GRIMM-2) of *Lesur et al.* [2010] is only resolved at large scales whereas any scale of the velocity field can contribute to this resolved SV. Finally, as it is the case for the SV, only the large-scale core MF can be determined at the Earth surface, yet interactions between the unknown small-scale MF with the VF can generate large-scale SV [see *Eymin and Hulot*, 2005].

As shown by *Backus* [1968], to reduce the nonuniqueness of the velocity field in this inverse problem, constraints have to be imposed on the flow behavior. Different formulations have been proposed over the past decades. This includes tangential-geostrophy, tangential-magnetostrophy, steady flow, columnar flow, helical flow, or purely toroidal flow (see *Holme* [2007] and *Finlay et al.* [2010] for exhaustive reviews of the different constraints usually applied and their physical implications). Nevertheless, these physical constraints are not sufficient to provide a unique flow solution [see *Chulliat and Hulot*, 2000, and references therein], and additional regularization assumptions have to be introduced in the problem [see *Holme*, 2007].

Although identified for more than 20 years [*Hulot et al.*, 1992], it is only recently that the effects of the unknown small-scale MF on the large-scale SV have been modeled in the inversion of the frozen flux approximation. In particular, two methods have given promising results, namely the ensemble approach of *Gillet et al.* [2009] and the iterative method of *Pais and Jault* [2008]. The philosophies of these two approaches is quite distinct from one another. Whereas in the method of *Gillet et al.* [2009], an ensemble of magnetic field containing small scales is generated and directly used to evaluate an ensemble of velocity field; in the method of *Pais and Jault* [2008], the effects of the unknown magnetic field is transposed into a modeling error which is iteratively estimated. In this study, we propose a development of these approaches in the context of Bayesian modeling.

In section 2, after describing the principle of derivation of the frozen flux equation, we recall the issue raised in the inversion of this equation by the truncated nature of the available MF. We then describe how to isolate the large scales of the MF and present the approximated dynamical equation, referred as Filtered Frozen Flux (FFF) equation, which determines the evolution of these large scales. At the end of the section, we present how to formulate the inverse problem in a Bayesian framework when variations of the MF around the prescribed one are allowed to occur. In section 3, tests on synthetic data are performed. In the first one, we evaluate the improvement brought by using the FFF equation in the inverse problem. In the second test, the Bayesian formalism developed in section 2 is considered to recover the velocity field from a set of artificially generated data, and the results are compared to the flow obtained with three other approaches. The methodology we developed is then used to determine the velocity field and its underlying uncertainties for the epoch 2005.0. Finally, we present our conclusions in section 4.

2. Governing Equations

2.1. The Frozen Flux Approximation

In this section, we introduce briefly the hypothesis necessary to derive the frozen flux approximation. For a more detailed description, see *Holme* [2007].

Outside the core, the geodynamo's MF $\mathbf{B}$ is irrotational; it can therefore be expressed through a potential ϕ according to the relation:

$$\mathbf{B} = -\nabla\phi \,. \tag{1}$$

As mentioned previously, the low conductivity of the mantle [*Velímský*, 2010] allows to evaluate the MF, and therefore, its radial component $B_r = -\partial_r\phi$ at the level of the core-mantle boundary. There its evolution is prescribed by the induction equation:

$$\partial_t B_r = -\nabla_{\mathbf{H}}(\mathbf{u}B_r) + \eta\,(\Delta\mathbf{B})\cdot\mathbf{e_r}\,, \tag{2}$$

with $\nabla_{\mathbf{H}}$ the horizontal divergence operator, $\mathbf{u}$ the two-dimensional velocity field, η the magnetic diffusivity, and $\mathbf{e_r}$ a radial unitary vector. Because for the Earth, on short period of time, the dissipation effects are dominated by advection effects [see *Holme*, 2007], and since our study is limited to single epoch inversion, the fluid can be considered as a perfect conductor. *Roberts and Scott* [1965] showed that under this assumption, known as the frozen flux (FF) approximation, the induction equation can be simplified as follows:

$$\partial_t B_r = -\nabla_{\mathbf{H}}(\mathbf{u}B_r)\,. \tag{3}$$

2.2. The Unresolved Scale Issue

To perform a consistent inversion of the frozen flux equation at the CMB, in addition to imposing a certain behavior to the flow and to regularizing it [see *Holme*, 2007; *Finlay et al.*, 2010], every scale composing the secular variation and the magnetic field must be known. Unfortunately, in the current models describing the spatiotemporal evolution of the Earth's magnetic field derived from satellite and observatory data, the resolution of both the SV and the MF is limited. For the GRIMM-2 model of *Lesur et al.* [2010], for example, the fields do not excess the degree 13 when expanded in spherical harmonics. So if $g_{l,m}$ corresponds to the spherical harmonics (SH) coefficient at degree l and order m associated with the scalar potential ϕ, such as follows:

$$\phi = R \sum_{l=0}^{l=+\infty} \sum_{m=-l}^{m=+l} \left(\frac{c}{r}\right)^{l+1} g_{l,m} Y_{l,m} \,, \tag{4}$$

where R is the core radius, and $Y_{l,m}$ is the Schmidt seminormalized SH; then according to equation (1), the available MF $B_r^<$, and its unknown part $B_r^>$ are respectively given by the following:

$$B_r^< = -\sum_{l=1}^{l=lc} (l+1) \sum_{m=-l}^{m=+l} g_{l,m}^< Y_{l,m} \tag{5}$$

$$B_r^> = -\sum_{l=lc+1}^{l=+\infty} (l+1) \sum_{m=-l}^{m=+l} g_{l,m}^> Y_{l,m} \,, \tag{6}$$

with lc the cutoff scale (which is equal to 13 for the MF provided by the GRIMM-2 model). Note that the total radial component of the MF corresponds to the sum of these two quantities.

To account for the truncated nature of the available MF and SV, the frozen flux approximation has to be rewritten as follows:

$$\partial_t B_r^< = -\left(\nabla_{\mathbf{H}}(\mathbf{u}B_r)\right)^< \tag{7}$$

$$= -\left(\nabla_{\mathbf{H}}\left(\mathbf{u}B_r^<\right)\right)^< - \left(\nabla_{\mathbf{H}}(\mathbf{u}B_r^>)\right)^< \,, \tag{8}$$

where the advection term, on the right-hand side of equation (8), is split into two parts, one depending on the resolved magnetic field and the other function of the undetermined field. *Hulot et al.* [1992] were the first to highlight the issue raised by the unknown part of the MF in the inversion of the FF equation. Nevertheless, because at this epoch the uncertainties on SV measurements were large, the contribution of the term $\left(\nabla_{\mathbf{H}}(\mathbf{u}B_r^>)\right)^<$ could be neglected in the inverse problem. The recent increase in quality of both the measurements and models describing the evolution of the core MF [see *Hulot et al.*, 2002] invalidate this latter statement, and *Eymin and Hulot* [2005] showed that the unresolved part of the MF could no longer be neglected anymore.

2.3. Parametrization of the Unresolved Magnetic Field

To model the effects of the unresolved part of the magnetic field on the large-scale secular variation, assumptions on this unknown field behavior have to be made. In particular, one can prescribe to it a certain energy spectrum. This operation can be performed, for instance, by extrapolating the spectrum associated with the resolved scales which is defined by the following:

$$E_{B^<}(l) = (l+1) \sum_{m=-l}^{m=l} \left(g_{l,m}^<\right)^2 \,. \tag{9}$$

The resulting spectrum $E_{B^>}$ can then be used to statistically model the unknown MF $B_r^>$. Following the development of *Hulot et al.* [1992] where the field is assumed to be isotropically distributed, the covariance of the coefficients $g_{l,m}^>$ is directly proportional to the extrapolated spectrum through the relation:

$$E\left[g_{l,m}^>, g_{l',m'}^>\right] = \frac{E_{B^>}(l)}{(l+1)(2l+1)} \delta(l-l')\delta(m-m') \,, \tag{10}$$

where $E[\ldots]$ corresponds to the mathematical expectation.

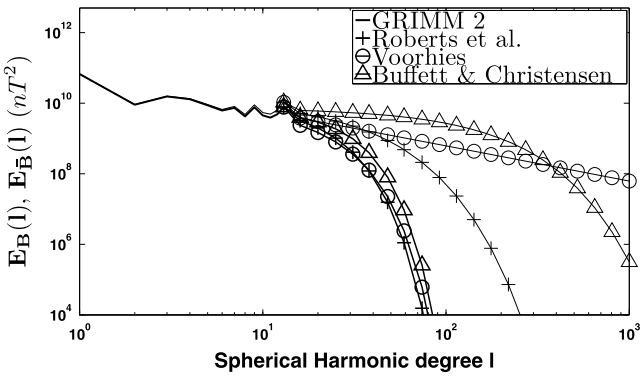

Figure 1. Energy spectrum of the GRIMM-2 magnetic field at the CMB for the epoch 2005.0 (between SH degree $1 \leq l \leq 13$) and its filtered (thick lines) and nonfiltered (thin lines) extrapolations. The laws used to extrapolate the large-scale spectrum were taken from *Roberts et al.* [2003] (plus symbols), *Voorhies* [2004] (circles), and *Buffett and Christensen* [2007] (triangles).

The issue with such a modeling is that no universal spectrum of the geodynamo's MF at the core mantle boundary is available. Nevertheless, different formulations have been proposed over the past decades, but unfortunately, most of them strongly differ from one another. An illustration of this statement is given in Figure 1 where the spectrum of the MF prescribed by the GRIMM-2 model for the epoch 2005.0 (between SH degree $1 \leq l \leq 13$) together with three different extrapolations (thin lines) are plotted. In this example, the laws derived by *Buffett and Christensen* [2007], *Roberts et al.* [2003], and *Voorhies* [2004] were used to extrapolate the resolved scale spectrum. They, respectively, read the following:

$$E_B^B(l) = C_1 \chi^l \tag{11}$$

$$E_B^R(l) = C_2 e^{-Sl} \tag{12}$$

$$E_B^V(l) = C_3 \frac{l + 1/2}{l(l+1)} \tag{13}$$

with $\chi = 0.99$ and $S = 0.055$. The constants C_1, C_2, and C_3 were determined by fitting the resolved magnetic field spectrum between the degree $2 < l \leq 13$.

As it is confirmed in Figure 1, the three extrapolated spectra present distinct behaviors. Furthermore, the law proposed by *Buffett and Christensen* [2007] predicts a strong concentration of energy at small scales. If this latter formulation was to be the closest one from reality, the unresolved MF would have to be modeled at very high degree (up to $l \sim 500$), which is nowadays numerically impossible. We propose therefore to reduce the impact of the small-scale magnetic field on the large-scale secular variation by applying a filter on the magnetic field and by determining the dynamical equation governing the evolution of the resulting filtered field.

2.4. Filtering of the Fields

As it is believed to be the case for the Earth's dynamo, the degree of turbulence in astrophysical or geophysical systems is most of the time extremely high. This implies that the magnetic and velocity fields are populated by a great variety of scales. Capturing all these scales in observations or in numerical simulations is usually impossible. Therefore, focusing on the large scales, and their dynamics, is probably the best solution to study such systems. This approach has been widely followed in the context of hydrodynamic (HD) and magnetohydrodynamic (MHD) turbulence [see *Sagaut*, 2006; *Lesieur*, 2008; *Baerenzung et al.*, 2008a, 2008b]; *Fabre and Balarac*, 2011]. To extract the large scales from a given field, one has to filter it. In HD or MHD turbulence, three different filters are generally used, the top-hat or the Gaussian filter for studies in Cartesian space, or the sharp cutoff filter in spectral space. While the top-hat and Gaussian filter are continuous filters, the cutoff filter truncates the field above a certain predefined scale. In spherical coordinates, the top-hat filter is usually preferred [*Sun and Su*, 2007] since until recently no equivalent of the Gaussian filter existed for such geometries (see, however, *Bülow* [2004]). In our study, we consider the isotropic filter developed by *Bülow* [2004]. The principle of derivation of this filter is detailed in Appendix A. Applying this filter to a scalar field ξ leads to the following:

$$\bar{\xi} = G \star \xi \,, \tag{14}$$

where $\overline{\xi}$ is the filtered field, the $\star$ symbol denotes the convolution product over the sphere between convolution kernel G and the scalar field ξ. According to the convolution theorem [see *Driscoll and Healy*, 1994], in spectral space equation (14) becomes the following:

$$\overline{\xi}_{l,m} = \sqrt{\frac{4\pi}{2l+1}}\xi_{l,m}G_l^0 , \tag{15}$$

where $\overline{\xi}_{l,m}$ and $\xi_{l,m}$ are, respectively, the filtered and the total SH coefficients associated with ξ, and G_l^0 is convolution kernel expressed in spectral space at degree l. Since for the filter developed by *Bülow* [2004], G is zonal, only its coefficients at order $m = 0$ are different from zero. As shown in Appendix A equation (A7), equation (15) can be expressed as follows:

$$\overline{\xi}_{l,m} = \xi_{l,m}\exp\left(-\frac{l(l+1)\overline{\Delta}^2}{24R^2}\right), \tag{16}$$

where $\overline{\Delta}$ corresponds to the filter width. With this formulation, one can directly connect the spectrum of the scalar field E_ξ to the spectrum of its filtered part $E_{\overline{\xi}}$ as follows:

$$E_{\overline{\xi}} = E_\xi \exp\left(-\frac{l(l+1)\overline{\Delta}^2}{12R^2}\right). \tag{17}$$

We then applied this filter to the three different extrapolated spectra presented in the previous section (see equations (11)–(13)). In Figure 1, the nonfiltered (thin lines) and the filtered (thick lines) spectra are plotted. The width of the filter has been set to $\overline{\Delta} = 500$ km in order to preserve the large-scale fields and to suppress the small-scale ones. One can observe that most of the energy that was contained in the small scales of the initial fields have now vanished in the filtered fields. Furthermore, the variations between the different extrapolated filtered spectra are now much less pronounced than in the nonfiltered case.

2.5. The Filtered Frozen Flux Approximation

Applying the spatial filter presented in the preceding section to the velocity and the magnetic field allows to decompose them into an averaged part $\overline{\mathbf{u}}$ and $\overline{B}_r$, and a fluctuating part $\mathbf{u}'$ and B_r' such as the following:

$$\mathbf{u} = \overline{\mathbf{u}} + \mathbf{u}' \tag{18}$$

$$B_r = \overline{B}_r + B_r' . \tag{19}$$

Since the spatial filter considered here is homogeneous and time invariant, it commutes with all the differential operators encountered in the induction equation. Therefore, applying this filter to the frozen flux approximation (equation (3)) leads to the following:

$$\partial_t \overline{B}_r = -\nabla_{\mathbf{H}}(\overline{\mathbf{u}\overline{B}_r}) . \tag{20}$$

Following the decomposition introduced by *Leonard* [1974], the part of the subgrid stress tensor which allows interactions between the tangential components of the velocity field and the radial component of the MF reads

$$\tau = \overline{\mathbf{u}\overline{B}_r} - \overline{\mathbf{u}}\overline{B}_r . \tag{21}$$

Now equation (20) can be rewritten as follows:

$$\partial_t \overline{B}_r = -\nabla_{\mathbf{H}}(\overline{\mathbf{u}}\overline{B}_r) - \nabla_{\mathbf{H}}\tau . \tag{22}$$

The subgrid stress tensor τ, through the averaged product $\overline{\mathbf{u}\overline{B}_r} = \overline{(\overline{\mathbf{u}} + u')(\overline{B}_r + B_r')}$, incorporates interactions between averaged and fluctuating part of the velocity and magnetic fields; thus, equation (22) is not closed in the sense that it does not only contains large-scale quantities. To close this equation, expressions of the fluctuating quantities depending on the averaged ones have to be derived.

As mentioned in Appendix A, the filtered velocity and magnetic field are both solutions of the diffusion equations:

$$\partial_s \mathbf{u}(\mathbf{x}, s) = D_u \Delta_H \mathbf{u}(\mathbf{x}, s) \tag{23}$$

$$\partial_s B_r(\mathbf{x}, s) = D_B \Delta_H B_r(\mathbf{x}, s) \tag{24}$$

$$\partial_s \left(\mathbf{u}(\mathbf{x}, s) B_r(\mathbf{x}, s)\right) = D_B \Delta_H \left(\mathbf{u}(\mathbf{x}, s) B_r(\mathbf{x}, s)\right) \tag{25}$$

where the filtered and total fields are, respectively, $\overline{\mathbf{u}} = \mathbf{u}(\mathbf{x}, s)$ and $\overline{B}_r = B_r(\mathbf{x}, s)$, and $\mathbf{u} = \mathbf{u}(\mathbf{x}, 0)$ and $B_r = B_r(\mathbf{x}, 0)$, and the product between s and the two diffusion coefficients D_B and D_u determines the width of the filter. Note that since D_B is the diffusion coefficient applied to each term of the frozen flux equation, it has to be applied to the MF but not necessarily to the VF. To link fluctuating to filtered fields, Taylor expansions at the first order in s of $\mathbf{u}$, B_r, and $\overline{\mathbf{u}B}_r$, using relations (23) to (25) are performed, leading to the following:

$$\mathbf{u} \sim \overline{\mathbf{u}} - sD_u \Delta_H \overline{\mathbf{u}} \tag{26}$$

$$B_r \sim \overline{B}_r - sD_B \Delta_H \overline{B}_r \tag{27}$$

$$\overline{\mathbf{u}B}_r \sim \mathbf{u}B_r + sD_B \Delta_H (\mathbf{u}B_r). \tag{28}$$

By analogy to the usual Gaussian filters used in large eddy simulations, one can define the following characteristic lengths:

$$\overline{\Delta}_u^2 = 24sD_u \tag{29}$$

$$\overline{\Delta}_B^2 = 24sD_B\,. \tag{30}$$

Letting $\overline{\Delta}_u^2 = \overline{\Delta}_B^2 = \overline{\Delta}^2$, injecting equations (26) and (27) into equation (28), and keeping only the first-order terms, one gets the following:

$$\overline{\mathbf{u}B}_r \sim \overline{\mathbf{u}}\overline{B}_r - \frac{\overline{\Delta}^2}{24}\left(\overline{\mathbf{u}}\Delta_H \overline{B}_r + \overline{B}_r \Delta_H \overline{\mathbf{u}} - \Delta_H(\overline{\mathbf{u}}\overline{B}_r)\right)\,, \tag{31}$$

which can be reduced to the following:

$$\overline{\mathbf{u}B}_r \sim \overline{\mathbf{u}}\overline{B}_r + \frac{\overline{\Delta}^2}{12}\left(\left(\nabla_{\mathbf{H}}\overline{B}_r\right)\nabla_{\mathbf{H}}\right)\overline{\mathbf{u}}\,. \tag{32}$$

So the subgrid stress tensor τ in its approximated closed form reads

$$\tau = \frac{\overline{\Delta}^2}{12}\left(\left(\nabla_{\mathbf{H}}\overline{B}_r\right)\nabla_{\mathbf{H}}\right)\overline{\mathbf{u}}\,. \tag{33}$$

The filtered frozen flux equation can now be written for the filtered secular variation $\partial_t \overline{B}_r^{<}$ truncated at degree $l_c = 13$ as follows:

$$\partial_t \overline{B}_r^{<} = -\left(\nabla_{\mathbf{H}}(\overline{\mathbf{u}}\overline{B}_r)\right)^{<} - \left(\nabla_{\mathbf{H}}\tau\right)^{<}\,, \tag{34}$$

with $\overline{B}_r = \overline{B}_r^{<} + \overline{B}_r^{>}$.

In the case where $\overline{\Delta}_u^2$ and $\overline{\Delta}_B^2$ are assumed to exhibit different values, the compact form of the subgrid stress tensor τ is lost. As a consequence, the numerical cost to evaluate this latter is increased. The simulations we performed in this study being numerically demanding, we therefore chose to set $\overline{\Delta}_u^2 = \overline{\Delta}_B^2$.

In our study, the extrapolated filtered magnetic field $\overline{B}_r^{>}$ is extended up to the spherical harmonic degree $l = 30$. Above this scale, the filtered magnetic field (for $\overline{\Delta} = 500$ km) is extremely weak (see Figure 1) and its influence on the large-scale secular variation is neglected.

2.6. Bayesian Formulation of the Inverse Problem

The problem of determining the velocity field at the CMB knowing the exact MF and the SV together with its uncertainties is an ill-posed inverse problem: in a continuum formulation, the number of unknown is twice as large as the number of equations. One of the most common methods to tackle this problem consists in minimizing an energy functional composed of two main terms; a quantity measuring the discrepancies between the model and the data, balanced, through a regularization parameter, with a quantity expressing a prior knowledge on the expected solution. This method has been widely used to evaluate the flow at the CMB and for a review of the different parametrization employed [see *Holme*, 2007].

Another option consists in formulating the problem in a Bayesian framework. The solution becomes then the full posterior distribution of the velocity field given the secular variation. This method allows the estimation of a model for the flow together with the quantification of its uncertainties.

When variations around the prescribed MF are allowed to occur, the inverse problem becomes more complicated. For models of the Earth's core MF derived from satellite or observatory data, the nature of these variations is diverse. At large scales, they can be due to a leakage of the external and lithospheric field into the core field, whereas at small scales, the entire MF is undetermined because of the dominance of the lithospheric field at the Earth's surface. Recent models such as GRIMM-2 [*Lesur et al.*, 2010] are able to separate at large scales (between SH degree $1 \leq l \leq 13$) the external from the core field, but not the lithospheric field from the core field. As a consequence, the large-scale lithospheric field becomes a source of uncertainty on the geodynamo's MF.

To parametrize the unresolved part of the MF in the inverse problem, different approaches have been recently developed. This includes the ensemble method of *Gillet et al.* [2009] and the iterative algorithm of *Pais and Jault* [2008]. In this study we propose to extend these methods to the context of Bayesian modeling, following the development of *Jackson* [1995]. Furthermore, in addition to parametrizing the unresolved MF, we also consider the uncertainties on the large-scale MF due to the lithospheric field.

2.6.1. CMB Velocity Distribution

From now on, in order to simplify the notations, the filtered MF and VF and the filtered and truncated SV will be written as follows:

$$\overline{B}_r = b \tag{35}$$

$$\overline{\mathbf{u}} = u \tag{36}$$

$$\dot{\overline{B}}_r^{<} = \gamma\,. \tag{37}$$

In this section, the distribution we want to characterize is the posterior distribution of the velocity field given the secular variation $p\,(u|\gamma)$. But since we want to account for the unknown small-scale magnetic field together with the uncertainties on the large-scale field, this distribution cannot be expressed directly. Nevertheless, it can be obtained by marginalizing the joint posterior distribution of the velocity field and the magnetic field as follows:

$$p\,(u|\gamma) = \int p(u, b|\gamma)\mathrm{d}b\,. \tag{38}$$

According to *Bayes* [1763], the distribution on the right-hand side of relation (38) can be decomposed into the following:

$$p(u, b|\gamma) = \frac{p(\gamma|u, b)p\,(u, b)}{p(\gamma)}\,, \tag{39}$$

with $p\,(u, b)$ the joint prior distribution of the VF and the MF, $p(\gamma)$ the distribution of the SV, which is constant with respect to both u and b, and finally $p(\gamma|u, b)$ the likelihood distribution. Because u and b are a priori assumed to be independent random variables, their joint distribution can be split into two distributions such as the following:

$$p\,(u, b) = p(u)p(b)\,. \tag{40}$$

The prior distribution of the VF $p(u)$ is assumed to be Gaussian with the following general form:

$$p(u) = \frac{\exp\left[-\frac{1}{2}u^T\Sigma_u^{-1}u\right]}{(2\pi)^{\frac{d}{2}}|\Sigma_u|^{\frac{1}{2}}} \tag{41}$$

with d the dimension of the VF vector, which in our case is twice as large as the dimension of the MF and SV, and Σ_u the velocity covariance matrix chosen to enforce the spatial smoothness of the flow. For this purpose, we impose that

$$u^T\Sigma_u^{-1}u = \int_\Omega \left(|\nabla_{\mathbf{H}}\left(\nabla_{\mathbf{H}}\cdot u\right)|^2 + |\nabla_{\mathbf{H}}\left(\mathbf{r}\times\nabla_{\mathbf{H}}\cdot u\right)|^2\right)\mathrm{d}\omega + \alpha^2\int_\Omega |u|^2\mathrm{d}\omega\,. \tag{42}$$

The right-hand side of equation (41) is composed of two different norms on u, namely the Bloxham's "strong norm" [*Bloxham*, 1988; *Jackson et al.*, 1993] for the first one and the standard L^2 norm for the second one. The domain of integration Ω is the surface of the sphere describing the CMB, and the balance factor α^2 is chosen to be small enough not to modify the correlation length induced by the Bloxham norm. Furthermore, the covariance is rescaled such as the averaged standard deviation of the velocity field intensity is 20 km/yr. This implies that at any location of the core-mantle boundary, the probability for the flow intensity to exceed the value of 50 km/yr, an upper limit calculated by *Finlay and Amit* [2011], is of the order of 0.01.

As for the velocity field, the magnetic field b is also assumed to be normally distributed, but with a mean b_0 corresponding to the resolved MF, and a covariance Σ_b. Its prior distribution can therefore be expressed as follows:

$$p(b) = \frac{\exp\left[-\frac{1}{2}\left(b-b_0\right)^T\Sigma_b^{-1}\left(b-b_0\right)\right]}{(2\pi)^{\frac{d}{4}}|\Sigma_b|^{\frac{1}{2}}}\,. \tag{43}$$

In this equation the two parts of the MF $b = b^< + b^>$ have different behaviors. The truncated field $b^<$ is taken from the GRIMM-2 model with $E[b^<] = b_0$ whereas the unknown MF $b^>$ is characterized by the averaged value $E[b^>] = 0$. Since in the GRIMM-2 model, the core field and the lithospheric field overlap at large scales, this latter field can be viewed as a source of uncertainties on $b^<$. We propose therefore to use the theoretical spectrum of the lithospheric field given by *Thebault and Vervelidou* [2013] to build the covariance matrix $\Sigma_{b^<}$ for the resolved scales magnetic field. This spectrum reads the following:

$$E_B^L(l) = (l+1)\left(\mu_0|M|F_l^a(\epsilon)\right)^2 l^{-\delta}C_l \tag{44}$$

with $|M| = 0.4225$ A m^{-1} the averaged crust magnetization, $\epsilon = 27$ km the equivalent magnetized layer thickness, and the constants $\mu_0 = 4\pi 10^{-7}$, $\delta = 1.28$, and $a = 6371.2$ km. The two functions $F_l^a(\epsilon)$ and C_l are given by the following:

$$C_l = \frac{l(l+1)(160l^5+264l^4-192l^3-130l^2+96l-9)}{6(2l+3)^2(2l+1)^2(2l-1)^2}$$
$$F_l^a(\epsilon) = \frac{1-(1-\epsilon/a)^{(l-1)}}{l-1}\,.$$

Letting the truncated MF $b^<$ being linked to its spectral counterpart $g_{l,m}^<$ through the relation $b^< = FPg_{l,m}^<$, where the operator P projects the coefficients in physical space, and the operator F filters the field, and assuming that the lithospheric field is isotropically distributed, the covariance of the truncated MF is the following:

$$\Sigma_{b^<} = E\left[\left(b^<-b_0\right)\left(b^<-b_0\right)^T\right] \tag{45}$$
$$= E\left[PF\left(g_{l,m}^<-g_{l,m}^0\right)\left(g_{l,m}^<-g_{l,m}^0\right)^T F^TP^T\right] \tag{46}$$
$$= PF\frac{E_B^L(l)}{(l+1)(2l+1)}F^TP^T\,, \tag{47}$$

where $g_{l,m}^0$ are the spherical harmonics coefficients associated with b_0.

The extrapolated SH coefficients of the MF $g^{>}_{l,m}$ are assumed to individually have a 0 mean and a variance depending on the extrapolated spectrum $E^{B}_{B^{>}}(l)$ from *Buffett and Christensen* [2007] as shown in equation (10). Therefore, in physical space, the MF also has a 0 mean at any spatial location and a covariance given by the following:

$$\Sigma_{b^{>}} = PF\frac{E^{B}_{B^{>}}(l)}{(l+1)(2l+1)}F^{T}P^{T}\,. \tag{48}$$

By combining $\Sigma_{b^{<}}$ with $\Sigma_{b^{>}}$, one gets the total covariance Σ_b for the MF.

The last distribution to characterize is the likelihood distribution which measures the discrepancies between the model (the filtered frozen flux equation) and the data (the secular variation). It reads the following:

$$p(\gamma|b,u) = \frac{\exp\left[-\frac{1}{2}\left(\gamma + A_u b\right)^{T}\Sigma_{\gamma}^{-1}\left(\gamma + A_u b\right)\right]}{(2\pi)^{\frac{d}{4}}|\Sigma_{\gamma}|^{\frac{1}{2}}}\,, \tag{49}$$

where the operator A_u, when applied to b, allows to calculate the nonlinear term of the filtered frozen flux equation $\left(\nabla_{\mathbf{H}}(ub+\tau)\right)^{<}$, and the covariance matrix Σ_{γ} is the SV posterior covariance of the GRIMM-2 model.

All the distributions entering the velocity field posterior distribution being detailed, this latter can be evaluated. The integral given in equation (38) has already been calculated by *Jackson* [1995], so we only present the result which reads as follows:

$$\begin{aligned} p(u|\gamma) &= \frac{p(u)}{p(\gamma)}\int p(\gamma|b,u)p(b)\mathrm{d}b \\ &\sim \frac{1}{|N|^{\frac{d}{4}}}\exp\left[-\frac{1}{2}\left(c - r^{T}N^{-1}r + u^{T}\Sigma_{u}^{-1}u\right)\right] \end{aligned} \tag{50}$$

with

$$N = A_u^{T}\Sigma_{\gamma}^{-1}A_u + \Sigma_b^{-1}\,, \tag{51}$$

$$r = \Sigma_b^{-1}b_0 - A_u^{T}\Sigma_{\gamma}^{-1}\gamma\,, \tag{52}$$

$$c = \gamma^{T}\Sigma_{\gamma}^{-1}\gamma + b_0^{T}\Sigma_b^{-1}b_0\,. \tag{53}$$

Since expression (50) does not allow an easy understanding of the effects arising from the modeling of the MF variations on the posterior distribution of the velocity field, we decided to rewrite it into a more intuitive form. It reads as follows:

$$\begin{aligned} p(u|\gamma) = &\frac{(2\pi)^{-\frac{3d}{4}}}{|\Sigma_{\tilde{\gamma}}|^{\frac{d}{4}}}\exp\left[-\frac{1}{2}\left(\gamma + A_u b_0\right)^{T}\Sigma_{\tilde{\gamma}}^{-1}\left(\gamma + A_u b_0\right)\right] \\ &\times\frac{1}{|\Sigma_u|^{\frac{d}{2}}}\exp\left[-\frac{1}{2}u^{T}\Sigma_u^{-1}u\right]\times\frac{1}{p(\gamma)} \end{aligned} \tag{54}$$

$$\Sigma_{\tilde{\gamma}} = \Sigma_{\gamma} + A_u\Sigma_b A_u^{T}\,. \tag{55}$$

This formulation is very similar to the posterior distribution of the velocity field in the case where the magnetic field is exactly known. Indeed, this latter distribution can be obtained by simply replacing the covariance matrix $\Sigma_{\tilde{\gamma}}$ by Σ_{γ}. One can therefore observe that accounting for the small-scale magnetic field and the lithospheric field when formulating the inverse problem in a Bayesian framework leads to an increase of the secular variation uncertainties through the quantity $A_u\Sigma_b A_u^{T}$. Because of the dependency of this latter term on the velocity field u, the maximum of the posterior distribution cannot be analytically calculated as already mentioned by *Jackson* [1995]. Nevertheless, it is numerically possible to extract the main statistical characteristics of this posterior distribution using a Markov chain Monte Carlo method [see *Mosegaard and Rygaard-Hjalsted*, 1999; *Rygaard-Hjalsted et al.*, 2000]. The algorithm we chose to explore the posterior distribution and the results we obtained are presented in the next section.

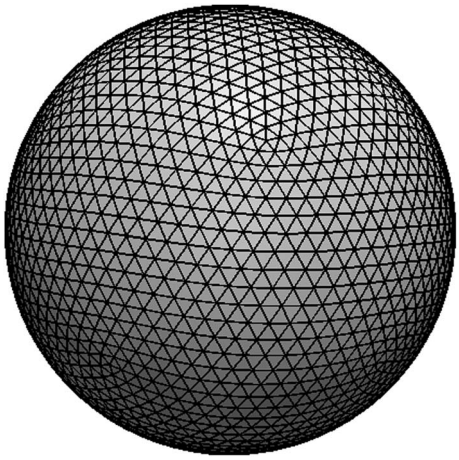

Figure 2. Discrete CMB after four steps in the refinement of the initial icosahedron.

3. Numerical Method and Results

The SV, MF, and VF are expressed in physical space; therefore, the surface of the CMB has been discretized by recursively dividing an initial icosahedron (see Figure 2). The grid construction and its properties, as well as the approximation of the differential operators are detailed in Appendix B.

Given that the grid is composed of N nodes, the vectors b, γ, and u are given by the following:

$$b^T = \left(b_0 ... b_i ... b_{N-1}\right) ,$$
$$\gamma^T = \left(\gamma_0 ... \gamma_i ... \gamma_{N-1}\right) ,$$
$$u^T = \left(u_0 ..., u_i, ..., u_{N-1}\right) .$$

3.1. Evaluation of the Filtered Frozen Flux Model

To evaluate the FFF model, an inversion of this equation was performed using GRIMM-2 as well as artificially generated MF and SV models. The large-scale magnetic field was taken from the GRIMM-2 model at the epoch 2001.0, whereas the small scales were randomly generated for SH degree lying between 14 and 160 according to the exponential law (11). The MF was then filtered (with $\overline{\Delta} = 80$ km) such as its smallest scales, which cannot be properly represented on the grid, exhibited a low-energy level. This MF is referred as b_0. To create a SV associated with this MF, we drew randomly a velocity field and used it to advect the MF with the FF equation (3). The velocity field was decomposed into a poloidal and a toroidal part such as the following:

$$\mathbf{u} = \nabla\Phi + \mathbf{e_r} \times \nabla\psi \ . \tag{56}$$

In spectral space, the spherical harmonics coefficients for the poloidal and toroidal field, respectively, read $\Phi_{l,m}$ and $\psi_{l,m}$. In order to promote interactions between small and large scales, $\Phi_{l,m}$ and $\psi_{l,m}$ were extended up to spherical harmonic degree 80 with the following statistical properties:

$$E[\Phi_{l,m}] = E[\psi_{l,m}] = 0 \quad \forall l, m \tag{57}$$

$$E[\Phi_{l,m}\Phi_{l',m'}] = Cl^{-14/3}|m|^{-11/3}\delta_{ll'}\delta_{mm'} \tag{58}$$

$$E[\psi_{l,m}\psi_{l',m'}] = Cl^{-14/3}|m|^{-11/3}\delta_{ll'}\delta_{mm'} \tag{59}$$

$$E[\Phi_{l,m}\psi_{l',m'}] = 0 \quad \forall l, l', m, m' \ , \tag{60}$$

where C is a normalization constant. The choice of a $l^{-14/3}$ power law imposed onto the poloidal and toroidal field correlation allowed to generate a flow with similar statistical properties than a two-dimensional turbulent flow [see *Sukoriansky et al.*, 2002].

To directly simulate the advection of the MF, a fourth-order Runge-Kutta scheme had been implemented. The integration time was taken to be 0.05 year, and the computation was performed on a grid refined 7 times (with 163, 842 nodes).

In Figure 3, the spectrum of the resulting secular variation is plotted. As it can be observed, the energy of the SV is maximum at scales lying between $l = 60$ and $l = 100$ indicating that the MF is strongly affected by the velocity field at these scales.

To mimic an analogous situation as the one encountered when using models fitting satellite data where both the MF and SV cannot be entirely taken into account, but in a less unfavorable case, the artificial fields were truncated at degree $l = 40$. The resulting MF and SV are respectively referred as γ and $b_0^<$. These fields were then used as an input for the inversion of the FFF equation. Two different filter widths were tested,

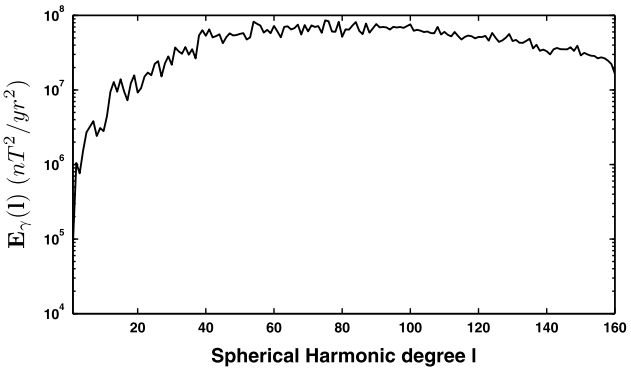

Figure 3. Spectrum of the secular variation generated by advecting the GRIMM-2 extrapolated MF at the epoch 2001.0 with an artificial velocity field.

$\overline{\Delta} = 500$ km and $\overline{\Delta} = 0$ km. Note that in the latter case, the equation reduces then to the usual FF approximation. Since the statistical properties of the velocity field were exactly known, they were directly injected in the prior information $p(u)$. No measurement errors on the secular variation and the magnetic field had been generated; therefore, the likelihood and the MF prior distributions, respectively, read as follows:

$$p(\gamma|u,b) = \delta\left(\gamma + \nabla_{\mathbf{H}}(bu+\tau)\right)\ , \quad (61)$$

$$p(b) = \delta(b - b_0^<)\ . \quad (62)$$

Multiplying together these two distributions and marginalizing the result with respect to b leads to the following:

$$p(\gamma|u) = \delta\left(\gamma + \nabla_{\mathbf{H}}\left(b_0^< u + \tau\left(b_0^<\right)\right)\right)\ , \quad (63)$$

with $\tau(b_0^<)$ the subgrid stress tensor evaluated with $b_0^<$. The posterior distribution of the velocity field is then proportional to:

$$p(u|\gamma) \sim p(\gamma|u)\,p(u)\ . \quad (64)$$

The Bayesian formulation of the problem being described, the discrete velocity field that maximizes the posterior distribution could be determined for the two cases. To do this, a particular solution of the equation $\gamma + \nabla_{\mathbf{H}}\left(b_0^< u + \tau\left(b_0^<\right)\right) = 0$ was calculated. In addition, the null space of the operator $A_{b_0^<}$ defined such as $A_{b_0^<}u = \nabla_H\left(b_0^< u + \tau\left(b_0^<\right)\right)$ was parametrized. The final solution corresponded then to the sum of the particular solution with the null space one which minimized the prior information on the VF. The grid used to realize the computation was composed of 10, 242 nodes (approximately 16 times less than the one taken to advect the MF). For the results to be comparable, the three different velocity fields were truncated at SH degree $l = 40$. Furthermore, the artificially generated field and the velocity field obtained by inverting the FF approximation ($\overline{\Delta} = 0$) were filtered with $\overline{\Delta} = 500$ km.

On the left side of Figure 4, the poloidal and toroidal spectra, respectively, defined by the following:

$$E_\Phi = l(l+1)\sum_{m=-l}^{m=l}(\Phi_{l,m})^2 \quad (65)$$

$$E_\psi = l(l+1)\sum_{m=-l}^{m=l}(\psi_{l,m})^2\ , \quad (66)$$

are plotted for the three velocity fields. The behavior of the spectra associated with the artificial velocity field (full line) is correctly reproduced at large scale ($1 \le l \le 23$) by both the FF (crosses) and the FFF (circles) flow models, whereas at SH degree close to the cutoff $l_c = 40$, the discrepancies between the exact spectra and the spectra of the inverted velocity fields become larger. Nevertheless, the spectra of the difference between exact and inverted velocity fields, displayed on the right side of Figure 4, show that the use of the FFF equation allows to reproduce more accurately the artificial velocity field at almost any scale.

To quantify the spatial error of the two inverted velocity fields, the following quantities were computed:

$$\mathcal{E}_{\mathrm{FF}} = \frac{\int |u - u_{\mathrm{FF}}|^2 \mathrm{d}\Omega}{\int \mathrm{d}\Omega} = 4,92\ \mathrm{km}^2.\,\mathrm{yr}^{-2} \quad (67)$$

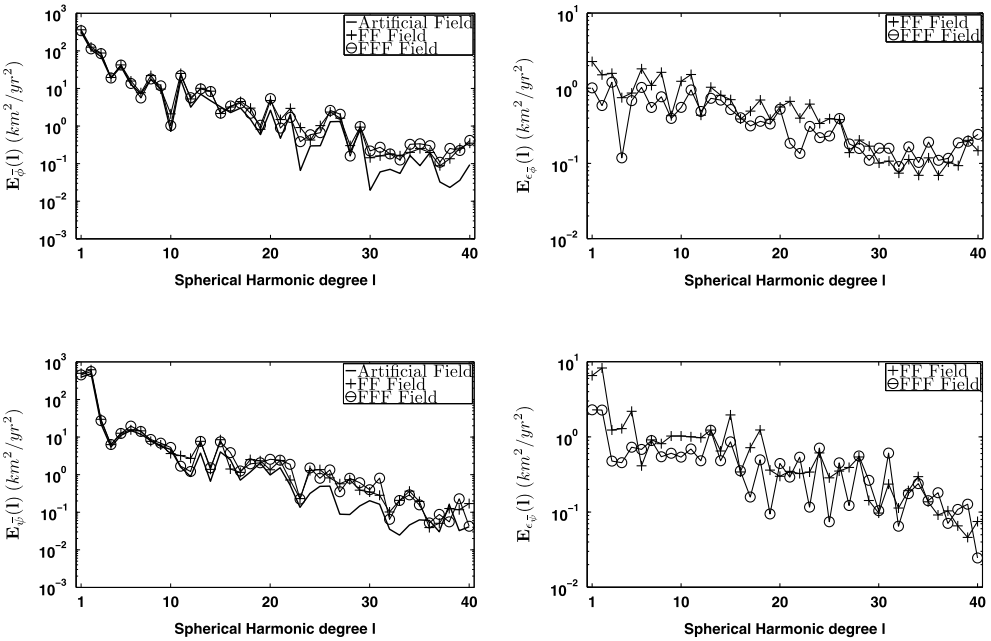

Figure 4. (top) Poloidal and (bottom) toroidal (left) energy spectra and (right) error spectra. The full line is associated with the exact field, the plus symbols correspond to the field solution of the FF inversion, and the circles are assigned to the field solution of the FFF inversion.

$$\mathcal{E}_{\mathrm{FFF}} = \frac{\int |u - u_{\mathrm{FFF}}|^2 \mathrm{d}\Omega}{\int \mathrm{d}\Omega} = 2,83 \text{ km}^2.\text{ yr}^{-2} \tag{68}$$

$$E_{\mathrm{tot}} = \frac{\int |u|^2 \mathrm{d}\Omega}{\int \mathrm{d}\Omega} = 130 \text{ km}^2.\text{ yr}^{-2}\,, \tag{69}$$

where the integration domain is the surface of the CMB, u is the exact filtered velocity field, u_{FF} and u_{FFF} are, respectively, the filtered velocity field obtained by inverting the FF and the FFF equations. The result of these computations shows that although the energy associated to the error fields is weak in comparison to the total energy of the exact flow, performing an inversion of FFF approximation reduces the global error on the VF.

3.2. Sampling of the Velocity Posterior Distribution

In this part we present a method to sample the posterior distribution $p(u|\gamma)$ given in equation (54). Since this distribution exhibits a complex form with respect to the velocity field u, directly drawing sample from it is impossible. Nevertheless, by building an appropriate Markov chain on the VF, one can map the distribution (for a complete description of Markov chain Monte Carlo methods, see *Gamerman and Lopes* [2006]). For this study we chose an algorithm of the Metropolis-Hastings type to construct the chain. The principle of the method is the following:

1. In the initial step, a VF u^n with $n = 0$ is generated. No particular property has to be imposed on this field, but choosing a field which is as close as possible to the one maximizing the target distribution will allow the chain to converge faster.
2. From u^n, a field u^{n+1} is constructed according to some arbitrary transition kernel $q(u^{n+1}, u^n)$.
3. The next step consists of accepting or rejecting the move from u^n to u^{n+1}. Therefore, an acceptance probability $\alpha(u^{n+1}, u^n)$ is defined. In the case of the Metropolis-Hastings algorithm, this probability is expressed as follows:

$$\alpha(u^{n+1}, u^n) = \min\left\{1, \frac{p(u^{n+1}|\gamma)q(u^{n+1}, u^n)}{p(u^n|\gamma)q(u^n, u^{n+1})}\right\}\,. \tag{70}$$

4. The process returns then to step 2 with u^{n+1} if the move from u^n to u^{n+1} is accepted, and with u^n otherwise.

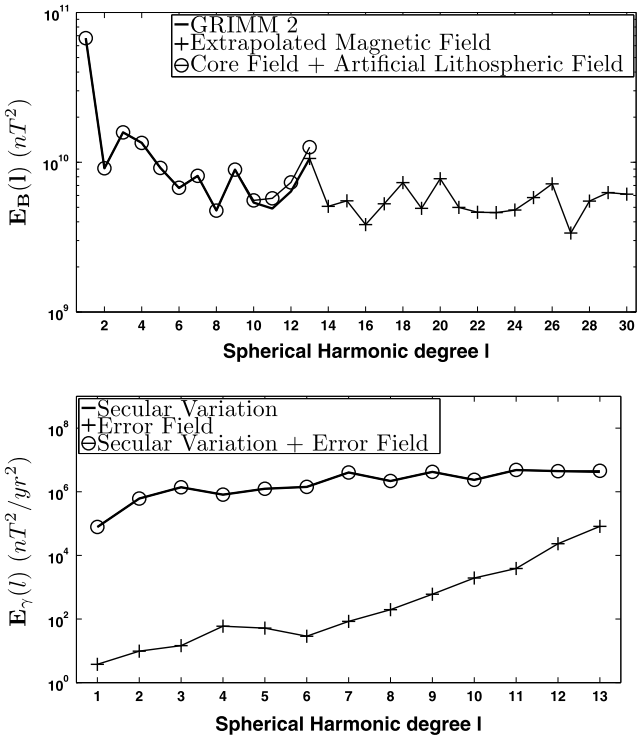

Figure 5. (top) Magnetic field energy spectra. GRIMM-2 MF for the epoch 2004.0 (thick line), extrapolated MF (plus symbols), and GRIMM-2 MF contaminated with a randomly generated lithospheric field (circles). (bottom) Secular variation energy spectra. Artificially generated SV (thick line), error field (plus symbols), and combination of the two fields (circles).

The ensemble is then assumed to be representative of the posterior distribution, once its averaged velocity field has converged towards a fixed vector.

Note that this algorithm has already been employed by *Mosegaard and Rygaard-Hjalsted* [1999]; *Rygaard-Hjalsted et al.* [2000] for sampling the posterior distribution given in equation (50), but with a different parametrization of the magnetic field and the velocity field. In particular, only the uncertainties on the large scale MF were considered in these two studies.

As already mentioned previously, analytically calculating the maximum of the posterior distribution $p(u|\gamma)$ is not feasible. We therefore decided to approximate it by taking the averaged VF of the ensemble generated by the Markov Chain, such as the following:

$$\arg\max_u p(u|\gamma) \sim \int u\, p(u|\gamma) \mathrm{d}u \,. \tag{71}$$

3.2.1. Evaluation and Comparison of the Method With Artificial Data

To evaluate our method, we generated artificially a secular variation field and a magnetic field and then performed the inversion of the FFF equation using these latter. We also compared our results to the ones obtained with alternative approaches. The construction of the synthetic fields was performed as follows:

Artificial magnetic field. The large-scale MF (between spherical harmonic degree $1 \leq l \leq 13$) was taken from the GRIMM-2 model at the epoch 2004.0. Its spectrum (the thick black line in Figure 5, top) was then extrapolated up to degree $l = 30$ according to the formulation (11) of *Buffett and Christensen* [2007]. From this small-scale spectrum, and under the assumption of isotropy and 0 mean of the field, a MF was randomly generated and added to the GRIMM-2 large-scale field. In Figure 5 (top), the spectrum of the small-scale MF is represented by the plus symbols.

Artificial velocity field. The coefficients, in spectral space, of the poloidal (Φ) and toroidal (ψ) fields were assumed to be isotropically distributed with a 0 mean and a covariance $\tilde{\Sigma}_u$ derived from the following power law spectrum:

$$E_\Phi(l) = E_\psi(l) = A^2 l^{-5/3} \,, \tag{72}$$

where the value of the amplitude A was chosen such as the averaged velocity intensity at the CMB was of 17 km yr^{-1}. The choice of an isotropic spectrum to characterize the flow behavior was dictated by usual inversion methods where the regularization term is derived under this hypothesis. A velocity field extending up to degree $l = 26$ was then randomly drawn accordingly to these statistical properties.

Artificial secular variation. To generate an artificial large-scale SV (extending up to degree $l = 13$), the MF was advected by the VF through the nonlinear term of the frozen flux approximation (3). The energy spectrum of the resulting SV is presented with the thick line in Figure 5 (bottom).

The next step of this evaluation was to recover the velocity field according to the magnetic field and the secular variation. But for this inverse problem to be more realistic, uncertainties were added to the data. A

large-scale lithospheric field ($1 \leq l \leq 13$) was randomly generated accordingly to the theoretical spectrum E_B^l of E. Thebault and F. Vervelidou (submitted manuscript, 2013) (see equation (44)) and added to the artificial MF. This contaminated field was then truncated at degree $l = 13$. It is referred as b_0 and its energy spectrum is plotted in Figure 5 (top) with circles. The uncertainties on the secular variation were built by randomly drawing a field from a Gaussian distribution with a 0 mean and a covariance given by the posterior covariance matrix of the GRIMM-2 secular variation Σ_γ. The resulting field was then superimposed on the artificial field. The spectrum associated with the total SV is shown with circles in Figure 5 (bottom).

Except for the prior distribution of the velocity field $p(u)$, all the distributions derived in section 2.6.1 are consistent to describe the posterior distribution of the velocity field in this test. We recall that they read the following:

$$p(\gamma|u,b) = \mathcal{N}\left(-\left(\nabla_{\mathbf{H}}\left(ub+\tau\right)\right)^{<}, \Sigma_\gamma\right), \tag{73}$$

$$p(b) = \mathcal{N}(b_0, \Sigma_b), \tag{74}$$

where $\mathcal{N}(x_0, \Sigma_x)$ corresponds to the normal distribution centered in x and with covariance Σ_x, and Σ_b is the covariance of the MF in which are included the uncertainties due to the lithospheric field and the modeling of the unresolved MF. For this evaluation phase, the prior distribution of the VF was given by the following:

$$p(u) = \mathcal{N}(0, \tilde{\Sigma}_u), \tag{75}$$

with $\tilde{\Sigma}_u$ the covariance of the VF derived from the power laws (72).

The estimation of the flow with respect to the artificial MF and SV was then realized with the five algorithms presented below.

MCMC method. In this approach, the full posterior distribution of the velocity field $p(u|\gamma)$ is explored with the Metropolis-Hastings algorithm described in the beginning of the section. The transition kernel $q(u^{n+1}, u^n)$ entering the algorithm (step 2) is derived from the prior distribution of the VF as follows:

$$q(u^{n+1}, u^n) = \frac{exp\left[-\frac{1}{2\lambda^2}(u^{n+1}-u^n)^T\tilde{\Sigma}_u^{-1}(u^{n+1}-u^n)\right]}{(2\pi)^{\frac{d}{2}}|\tilde{\Sigma}_u|^{\frac{1}{2}}}, \tag{76}$$

where the factor λ allows to rescale the covariance $\tilde{\Sigma}_u$ in order to limit the distance of the move from one velocity field to the other. Since this kernel is symmetric with respect to u^{n+1} and u^n, the acceptance probability $\alpha(u^{n+1}, u^n)$ of equation (70) reduces to the following:

$$\alpha(u^{n+1}, u^n) = \min\left\{1, \frac{p(u^{n+1}|\gamma)}{p(u^n|\gamma)}\right\}. \tag{77}$$

The initial field was set to 0 and an ensemble of $N_m = 230,000$ VF u_i was generated. We then approximated the flow maximizing the posterior distribution through the averaging operation:

$$u_0 = \frac{1}{N_m}\sum_{i=1}^{i=N_m} u_i. \tag{78}$$

Least square method. In this method, the magnetic field b is assumed to be exactly known such as the following:

$$p(b) = \delta(b - b_0). \tag{79}$$

As a consequence, the posterior distribution of the velocity field becomes proportional to the following:

$$p(u|\gamma) \sim \exp\left[-\frac{1}{2}\left(\gamma + A_{b_0}u\right)^T\Sigma_\gamma^{-1}\left(\gamma + A_{b_0}u\right)\right] \times \exp\left[-\frac{1}{2}u^T\tilde{\Sigma}_u^{-1}u\right], \tag{80}$$

where A_{b_0} is the operator allowing to evaluate the nonlinear term of the FFF equation when it is applied to u. The maximum of this distribution can be calculated analytically and corresponds to the usual least square solution as follows:

$$u_0 = -(A_{b_0}^T \Sigma_\gamma^{-1} A_{b_0} + \tilde{\Sigma}_u^{-1})^{-1} A_{b_0}^T \Sigma_\gamma^{-1} \gamma \,. \tag{81}$$

Ensemble method. This approach was developed by *Gillet et al.* [2009] and consists in generating an ensemble of magnetic field and calculating their associated velocity field. In this test, the ensemble of MF was randomly drawn from the distribution $p(b)$ given in equation (74). In total, we generated $N_e = 100$ magnetic fields b_i (with $1..i..N_e$) extending up to degree $l = 30$. Each velocity field u_i was then determined by the relation:

$$u_i = -(A_{b_i}^T \Sigma_\gamma^{-1} A_{b_i} + \tilde{\Sigma}_u^{-1})^{-1} A_{b_i}^T \Sigma_\gamma^{-1} \gamma \,. \tag{82}$$

where the operator A_b now depends on each realization b_i of the magnetic field. The flow solution of the complete inverse problem is given by the following:

$$u_0 = \frac{1}{N_e} \sum_{i=1}^{i=N_e} u_i \,. \tag{83}$$

Iterative method. In this approach, *Lesur et al.* [2013] proposed to determine the CMB velocity field through the following iterative process:

$$u^{n+1} = -(A_{b_0}^T \left(\Sigma_{\tilde{\gamma}}^n\right)^{-1} A_{b_0} + \tilde{\Sigma}_u^{-1})^{-1} A_{b_0}^T \left(\Sigma_{\tilde{\gamma}}^n\right)^{-1} \gamma \tag{84}$$

where n is the index of the iteration, and the covariance $\Sigma_{\tilde{\gamma}}^n$ is given by the following:

$$\Sigma_{\tilde{\gamma}}^n = \Sigma_\gamma + \left(A_{u^n}\right) \Sigma_b \left(A_{u^n}\right)^T \tag{85}$$

with A_{u^n} the operator depending on the velocity field u^n, and which allows to evaluate the nonlinear term of the FFF equation when it is applied to b. In the numerical implementation of this method, the initial field u^0 was taken as the one solution of the least square approach.

Note that this algorithm provides an estimation of the maximum of the posterior distribution given in equation (54) if the quantity $A_u \Sigma_b A_u$ is assumed to vary slowly with respect to u.

Iterative (Bloxham). To evaluate the impact of the velocity field prior information on the solution of the inverse problem, we implemented the iterative method introduced in the previous paragraph with a different covariance matrix for the velocity field. Instead of taking into account $\tilde{\Sigma}_u$ given in equation (84), we considered the covariance matrix Σ_u based on the Bloxham "strong norm," and defined in section 2.6.1 equation (41).

In the previous section, we mentioned the algorithm of *Pais and Jault* [2008] which also allows to take into account the variations of the MF in the inverse problem. We decided not to implement it in this evaluation since it is an approximation of the method proposed by *Lesur et al.* [2013].

To compare the different approaches, the artificial velocity field u is decomposed into a toroidal (ψ) and a poloidal (Φ) field, with $\psi_{l,m}$ and $\Phi_{l,m}$ their respective spectral counterpart. The same operation is performed on the velocity fields u_0 given by the four inversion methods. Their toroidal and poloidal parts are then referred as ψ_0 and Φ_0 in physical space, and $\psi_{l,m}^0$ and $\Phi_{l,m}^0$ in spectral space.

We recall that to perform these different inversions, the artificial secular variation and the artificial magnetic field are truncated at spherical harmonic degree $l = 13$, the velocity field is extended up to degree $l = 26$, and the covariance matrix for the magnetic field (when taken into account) is defined up to degree $l = 30$. The filter width $\overline{\Delta}$ is set to 500 km.

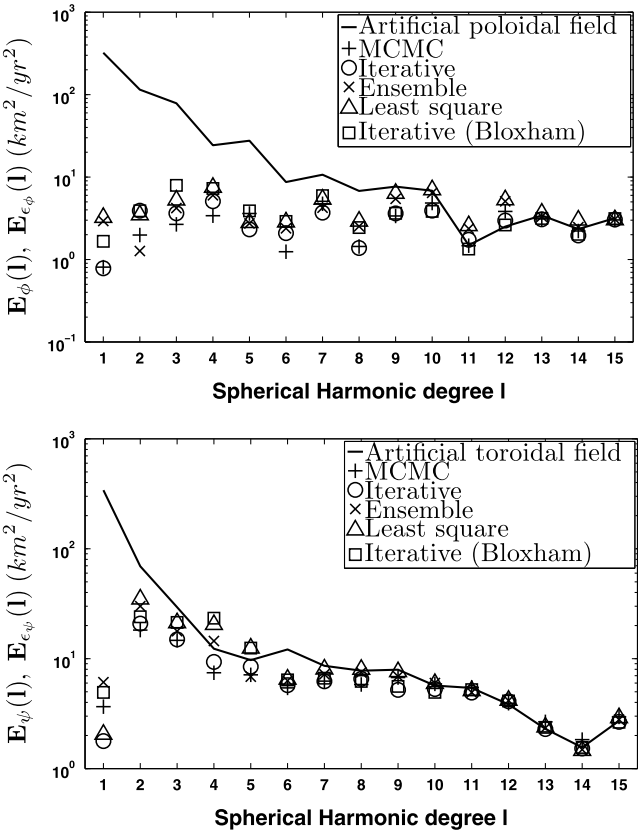

Figure 6. (top) Poloidal and (bottom) toroidal energy spectra for the artificial VF (thick lines) and for the different error fields (symbols).

To measure the accuracy of the various velocity fields, we define the poloidal and toroidal error fields as follows:

$$\epsilon^{\Phi}_{l,m} = \Phi_{l,m} - \Phi^0_{l,m} \tag{86}$$

$$\epsilon^{\psi}_{l,m} = \psi_{l,m} - \psi^0_{l,m}\,, \tag{87}$$

and their associated energy spectra as follows:

$$E_{\epsilon_\Phi} = l(l+1)\sum_{m=-l}^{m=l}(\epsilon^{\Phi}_{l,m})^2 \tag{88}$$

$$E_{\epsilon_\psi} = l(l+1)\sum_{m=-l}^{m=l}(\epsilon^{\psi}_{l,m})^2\,. \tag{89}$$

In Figure 6, the spectra of the error fields (symbols) are plotted together with the poloidal and toroidal spectra of the artificial velocity field (solid lines). The first observation one can make is that above the SH degree $l = 10$, the energy associated with the error fields is of the same order than the energy of the artificial poloidal and toroidal fields. This implies that above this degree, the estimation of the flow is not reliable whatever the method employed to determine it. At large scale, the performance of the different approaches varies strongly. Whereas the flow obtained with the least square method (triangles) is the one which deviates the most from the artificial flow, the velocity fields evaluated with the iterative method (circles) and the MCMC algorithm (plus symbols) are the ones presenting the lowest error intensities. In between, in terms of accuracy, lies the ensemble method (crosses), and the iterative method with prior velocity covariances based on the Bloxham's strong norm (squares). For this latter approach, whereas at very large scales, the level of error ($1 \leq l \leq 7$) is comparable to the one observed in the least square case; above degree 7, the error energies diminish and coincide with the ones the MCMC and iterative flows exhibit. It can be noticed that at degree $l = 4$ for the ensemble method and between $l = 4$ and $l = 5$ for the least square and iterative (Bloxham) methods, the energy associated with the toroidal error field is larger than the energy of the artificial velocity field itself. This is not the case anymore when using the iterative or MCMC approaches.

To evaluate the different models in physical space, the coefficients associated with the poloidal and toroidal error fields (equations (86) and (87)) were truncated at degree $l = 10$, since at smallest scales the uncertainties are maximal and projected in real space. Figure 7 shows the intensity of these velocity fields at the level of the CMB below America for the five approaches. Although the locations of the errors are similar, their intensities differs strongly from one flow to the other. A computation of the averaged energy associated with the poloidal and toroidal error fields (see Table 1) shows that globally, the best approximation of the artificial velocity field is provided by the MCMC algorithm, followed in order by the iterative, ensemble, iterative (Bloxham), and least square methods. Note that the differences between the MCMC and iterative approach are very low, and since the computation time required to sample the full posterior distribution is much larger than the one to approximate its maximum with the iterative method, if one wants to determine the flow without its underlying uncertainties, using the algorithm of *Lesur et al.* [2013] is certainly more appropriate.

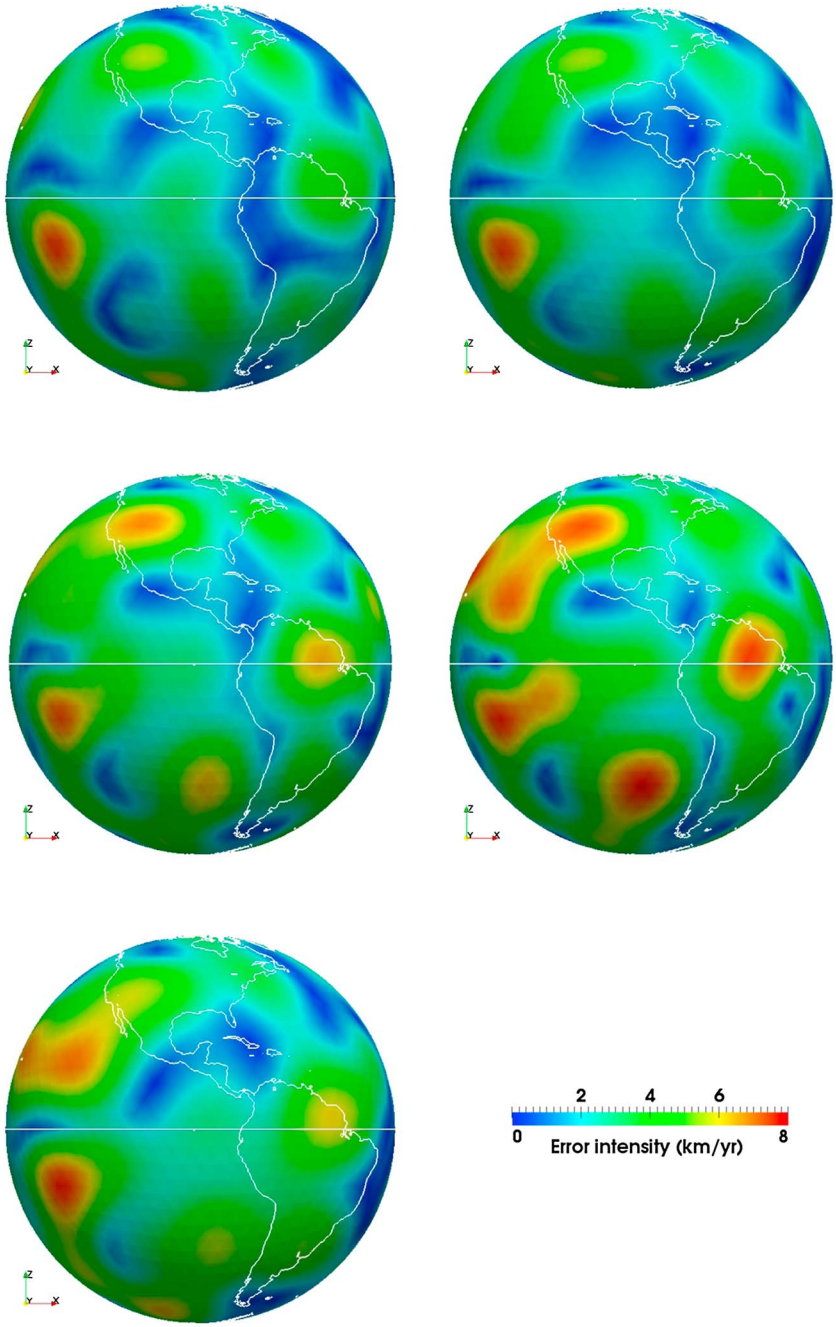

Figure 7. Intensity, in km yr^{-1}, of the difference between the artificial velocity field and the velocity fields evaluated with the following approaches: (top left) MCMC, iterative (top right) from *Lesur et al.* [2013] ensemble (middle left) from *Gillet et al.* [2009], (middle right) least square, and (bottom left) iterative with velocity prior covariances based on the Bloxham's strong norm.

Since the MCMC algorithm provides an information on the flow uncertainties, we extracted the standard deviation of the velocity intensity $\sigma|u|$, from the variance σ_u^2 as following:

$$\sigma_u^2 = \int \mathrm{diag}\left[\left(u-u_0\right)\left(u-u_0\right)^T\right] p(u|\gamma)\mathrm{d}u \tag{90}$$

where the term diag means that only the diagonal elements of the matrix lying within the brackets are kept. At each node of the discrete CMB, the VF u is composed of a polar and an azimuthal component, so to get the variance associated with the velocity intensity $\sigma_{|u|}^2$, the variance of each component has to be summed

Table 1. Averaged Energy of the Error in km^2 yr^{-2} Associated With the Different Inverted Velocity Fields[a]

	MCMC	Iterative	Ensemble	Least Square	Iterative (Bloxham)
Poloidal Field	2.20	2.42	3.04	3.72	3.45
Toroidal Field	6.45	6.72	8.69	10.1	9.23

[a]These values have to be compared with the averaged energies of the artificial poloidal and toroidal fields which are, respectively, of 48.07 km^2 yr^{-2} and 45.28 km^2 yr^{-2}.

up. In Figure 8 (left), the quantity $2\sigma_{|u|}$, corresponding to the 95% confidence interval on the flow intensity, is displayed in the region of the CMB below America. This picture presents a pessimistic view of the uncertainties to be expected when evaluating the flow maximizing the posterior distribution. Because the probability for the real flow to lie within the tails of the posterior distribution is very low, the predicted error will globally be larger than the effective one. Nevertheless, locations where the differences between the solution flow and the real one are important in corresponding to areas of high posterior variance.

In spectral space, the MCMC ensemble of velocity fields is used to evaluate the scale-by-scale variance of the poloidal and toroidal flow components, respectively, $\sigma^2_\Phi(l)$ and $\sigma^2_\Psi(l)$. After rescaling these quantities by the factor $l(l+1)$, they were plotted, in Figure 8 (right), together with the poloidal (Figure 8, right, top) and toroidal (Figure 8, right, bottom) spectra of the artificial velocity field (black lines) and the MCMC error fields (plus symbols). On this figure, it can be seen that although the variance cannot exactly describe the effective error associated with the MCMC flow, it allows a good estimation of the velocity field uncertainties to be expected. It can also be observed that according to the sample of the posterior distribution, the reliability of the toroidal field is questioned at very low SH degree ($l \geq 5$).

Different conclusions can be drawn from this evaluation phase. First, modeling the unresolved part of the magnetic field when performing the inversion of the FFF equation allows to considerably improve the accuracy, at any scale, of the calculated flow. Then, this test showed that at large scales (up to SH degree $l = 10$), the posterior distribution is dominated by the likelihood distribution, whereas at small scales, the prior distribution prevails. This is why the evaluation of the flow with a "wrong" prior velocity covariance matrix remains acceptable. Finally, we could demonstrate that the MCMC algorithm we developed to explore the posterior distribution is an appropriate tool to quantify the flow uncertainties.

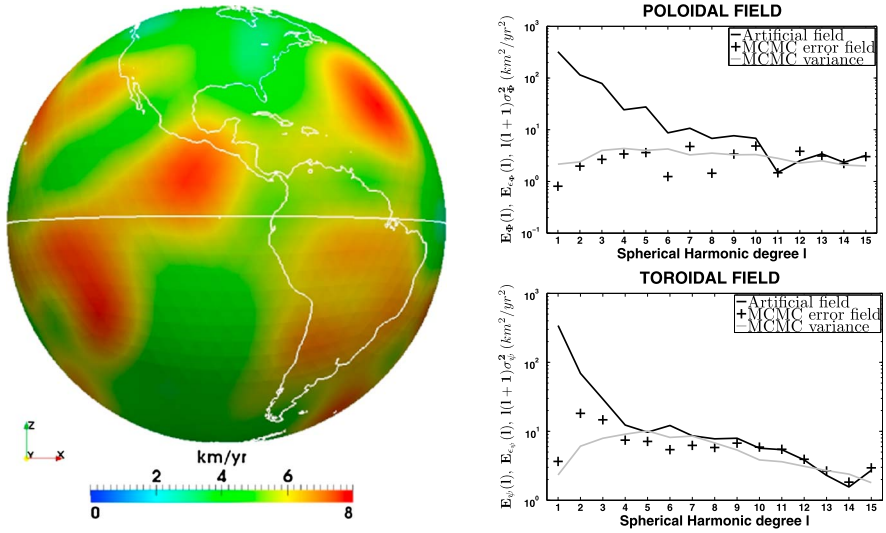

Figure 8. (left) 95% confidence interval on the velocity intensity in km yr^{-1} according to the MCMC flow ensemble. (right, top) Poloidal and (right, bottom) toroidal spectra of the artificial velocity field (black lines), spectra of the MCMC error fields (plus symbols), and rescaled scale-by-scale variance deriving from the MCMC flow ensemble (gray lines).

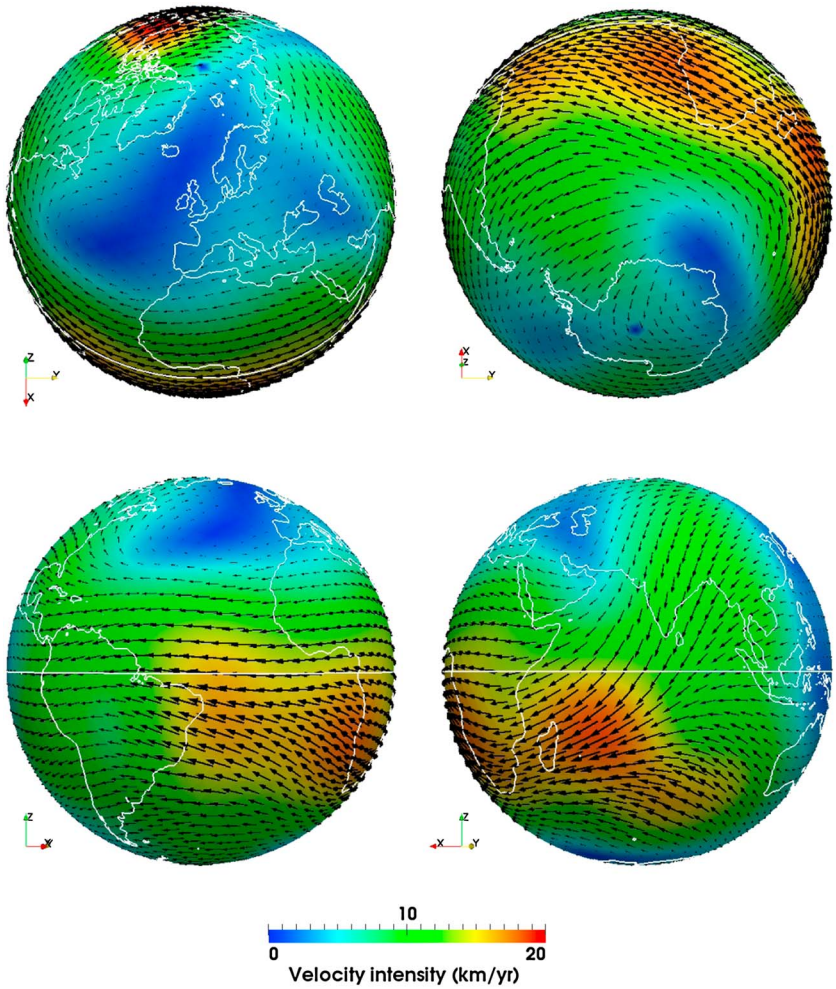

Figure 9. Velocity field $\hat{u}$ and its intensity for the epoch 2005.0.

3.2.2. Application of the MCMC Algorithm for the Epoch 2005.0

In the flow calculation, we realized, the MF and the SV as well as the covariance for the SV, are given up to SH degree $l = 13$ by the GRIMM-2 model of *Lesur et al.* [2010] for the epoch 2005.0. For the magnetic field, the covariance associated with its large scales ($0 < l \leq 13$) is derived from the theoretical spectrum of the lithospheric field of E. Thebault and F. Vervelidou (submitted manuscript, 2013) as shown in equations (44)–(47), whereas the extrapolation of the MF spectrum proposed by *Buffett and Christensen* [2007] is used to build the covariance matrix of the small-scale MF ($13 < l \leq 30$) as presented in equation (48). The velocity field is extended up to SH degree $l = 26$, and its prior distribution is given by the relation (41). The width of the filter has been set to $\overline{\Delta} = 500$ km, and the initial field of the Markov chain u_0 is the velocity field solution of the least square approach:

$$u_0 = -\left(A_B^T \Sigma_\gamma^{-1} A_B + \Sigma_u^{-1}\right)^{-1} A_B^T \Sigma_\gamma^{-1} \gamma \tag{91}$$

with $A_B u = \left(\nabla_{\mathbf{H}} (ub + \tau)\right)^<$.

As for the synthetic test of section 3.2.1, the transition kernel $q(u^{n+1}, u^n)$ was derived from the prior distribution of the VF as shown in equation (76).

The Metropolis-Hastings algorithm was then numerically simulated on a discrete CMB refined 4 times. An ensemble of 130, 000 VF u mapping the posterior distribution have been generated. The velocity field $\hat{u}$ maximizing the posterior is approximated by taking the average velocity field of the ensemble we created.

In Figure 9, the vector field $\hat{u}$ and its intensity are displayed in different locations of the core-mantle boundary. Many features of the flow we obtained have already been reported in previous studies. In particular, the

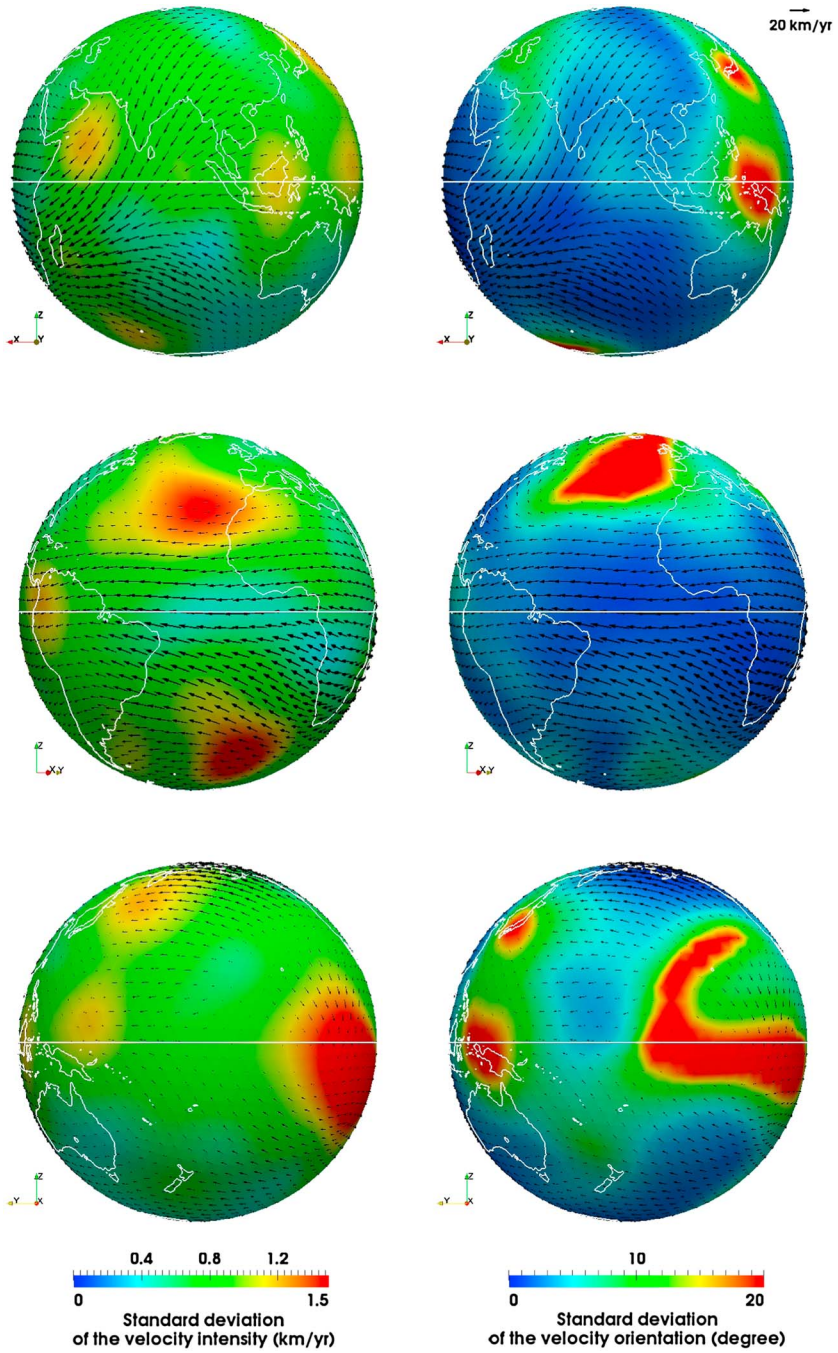

Figure 10. Velocity field $\hat{u}$ for the epoch 2005.0 and its associated uncertainties on (left) the intensity $\sigma_{|u|}$ in km yr^{-1} and (right) orientation σ_Γ in degree.

eccentric and planetary scale anticyclonic gyre observed by *Pais and Jault* [2008] and *Gillet et al.* [2009] is also present in the flow we calculated. This observation reinforces the hypothesis that the fluid motions in the outer core can be well described by the compressible quasi-geostrophic assumption, a constraint a priori applied in both studies. Nevertheless, according to our results, deviations from quasi-geostrophy have also to be expected. Indeed, under this hypothesis, the flow is forced to be symmetric with respect to the equator outside the tangential cylinder, a condition which is not fulfilled everywhere in our case. Although the symmetric part of the velocity field is dominant in our simulation (82% of the energy of the total VF is concentrated in its symmetric components), certain patterns such as the flow crossing the equator below India or the larger intensity of the westward drift in the Southern Hemisphere are violating this property.

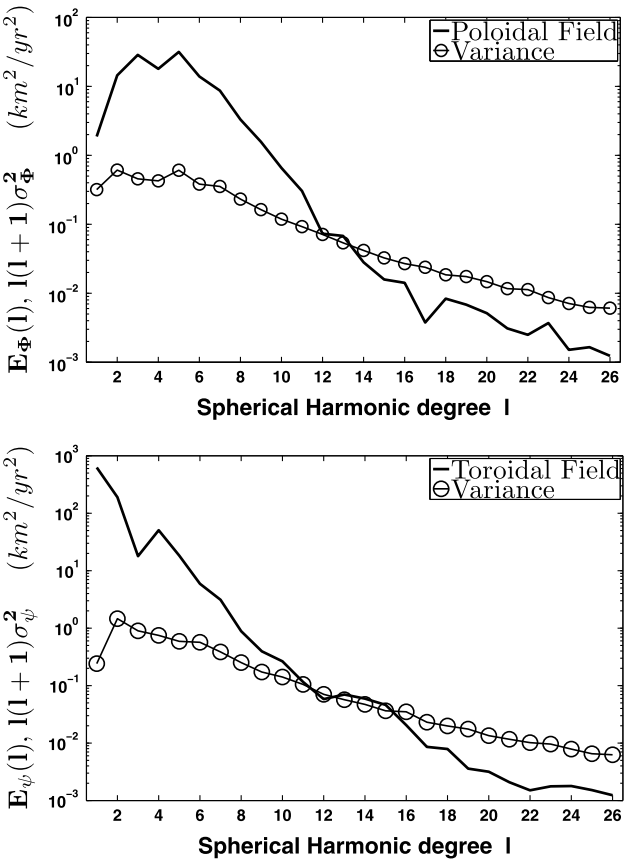

Figure 11. (top) Poloidal and (bottom) toroidal energy spectra associated with the velocity field $\hat{u}$ (thick line), and with the spectral uncertainties (circles).

The flow we obtained also exhibits a much smoother spatial behavior than the ones presented by *Pais and Jault* [2008] and *Gillet et al.* [2009]. This is certainly due to the choice we made to characterize a priori the velocity field. Through the Bloxham's strong norm, we imposed a very steep spectrum (in l^{-5}) to both the poloidal and toroidal field; as a consequence, the intermediate scales of the VF were probably overdamped in our simulation.

Possessing the full posterior distribution of the VF allows the extraction of much useful information on the flow. In particular, the uncertainties on the velocity field intensity and orientation (with respect of course to the prescribed modeling) can be evaluated at any spatial location on the grid. To compute the standard deviation of the velocity field intensity $\sigma_{|u|}$, we followed the protocol given in section 3.2.1, whereas the standard deviation of the velocity orientation σ_Γ is derived from the formula:

$$\sigma_\Gamma^2 = \int diag\left[\Gamma\Gamma^T\right] p(u|\gamma)\mathrm{d}u\,, \quad (92)$$

where Γ is the angle, in degree, between the velocity field u and $\hat{u}$. The quantities $\sigma_{|u|}$ and σ_Γ are displayed in Figure 10 (on the left for the $\sigma_{|u|}$ and on the right for the σ_Γ). This figure first shows that a strong (respectively weak) uncertainty on the intensity coincides with a strong (resp. weak) uncertainty on the orientation of the flow. Second, one can notice that the uncertainties are not homogeneously distributed on the surface of the CMB. While the planetary scale eccentric gyre seems to be very robust, the VF in the region of the CMB below the Pacific Ocean is much more uncertain. It is known that in this latter area, the magnetic field activity is moderate [*Hulot et al.*, 2002]. As a consequence, the secular variation is low, and its associated uncertainties, due to the inaccuracy of the measurements and to the interactions between the unresolved MF and the VF, may be larger than the signal itself. It is therefore very difficult to evaluate the velocity field in this region. Nevertheless, this figure shows that there is a large part east of Australia and around the longitude of New Zealand where the VF can be accurately estimated under our prior assumptions. Another particular feature can be noticed at the level of the North-Atlantic ocean, where the uncertainties on both the flow intensity and orientation are very large. As already questioned by *Finlay et al.* [2010], the robustness of the clockwise gyre usually observed in this area by models assuming tangential-geostrophy seems to be very weak according to our results.

Since we are using truncated MF and SV, it may be interesting to investigate the spectral properties of the posterior VF. The poloidal Φ and toroidal ψ part of the VF u are expanded in spherical harmonics. The resulting fields are, respectively, referred as $\Phi_{l,m}$ and $\psi_{l,m}$. The same operation is performed on $\hat{u} = \boldsymbol{\nabla}\hat{\Phi} + \mathbf{e_r} \times \boldsymbol{\nabla}\hat{\psi}$, with $\hat{\Phi}_{l,m}$ and $\hat{\psi}_{l,m}$ its poloidal and toroidal SH coefficients. In Figure 11 are plotted the spectra associated with $\hat{\Phi}_{l,m}$ and $\hat{\psi}_{l,m}$ and the variance on these coefficient summed up over the order m and rescaled by the factor $l(l+1)$. We can observe that the largest scales of the flow are dominated by its toroidal part. A computation of the poloidal and toroidal energy shows that more than 88% of the total energy is of toroidal nature. The other information which can be extracted from Figure 11 is that, as for the synthetic test we realized previously, above the SH degree $l = 10$, the intensity of the flow uncertainties becomes larger than the intensity

of the flow itself. As a consequence, the evaluation of the small-scale velocity field cannot be considered as reliable. For the largest velocity scales ($1 \leq l \leq 10$), the uncertainties exhibit a very low level of intensity, particularly when these latter are compared to the ones observed in the synthetic case (see Figure 8). This is certainly a consequence of the strong regularization constraint we employed and the rescaling factor we applied to it.

It has to be emphasized that all the results we obtained are conditioned by the choice of the prior information imposed to the flow and should not be considered as absolute.

4. Conclusions

In this study we have presented a new method to determine the velocity field at the Earth's core mantle boundary according to an outer core magnetic field and secular variation model. We showed that using an appropriate dynamical equation to prescribe the large-scale magnetic field evolution in the inverse problem, permitted to reduce the modeling errors arising from the truncated nature of the available fields. We also demonstrated that the Bayesian formalism we developed to account for the large-scale uncertainties on the magnetic field and to model the unresolved small-scale MF, allowed to properly describe the inverse problem as soon as the information introduced a priori were accurate. Through the evaluation of our method and the comparison with other approaches, we could indirectly confirm that the unresolved part of the magnetic field contributed significantly to the observed secular variation and that its modeling was necessary to obtain a more accurate description of the flow at the core-mantle boundary.

When we applied our method to the GRIMM-2 magnetic field and secular variation models for the epoch 2005.0, we could recover many features of the flow already observed in previous studies where a different prior information on the velocity field had been considered. In particular, we could retrieve the planetary scale eccentric gyre characteristic of flow evaluated under the compressible quasi-geostrophy assumption [see *Pais and Jault*, 2008; *Gillet et al.*, 2009]. Nevertheless, according to our simulation, the flow crosses the equator below India and the intensity of the westward drift is the larger in the Southern Hemisphere, indicating that the equatorial symmetry imposed by the quasi-geostrophy hypothesis is broken. Through this observation, one can conclude that deviations from quasi-geostrophy should be allowed to occur when this latter constraint is imposed in the inverse problem. Another specific feature of the velocity field we obtained is its very smooth spatial behavior. This property is certainly induced by the prior distribution of the velocity field we chose, since this latter imposes a very steep spectrum to both the poloidal and toroidal part of the velocity field.

Finally, thanks to the ensemble of velocity field we generated to map the posterior distribution, we could evaluate the uncertainties, depending nevertheless on the prior assumptions we chose, of the flow solution of the inverse problem. According to our results, whereas on the one hand, the robustness of the flow is questioned in many area, and particularly in almost the entire Pacific Ocean, and in the northern part of the Atlantic Ocean, on the other hand, the planetary scale eccentric gyre seems to be a very robust structure. From the evaluation of the uncertainties in spectral space, we could confirm that the flow at the CMB could only be accurately estimated at large scales (between spherical harmonics degree 1 and 10).

Appendix A: Spherical Diffusion

In Cartesian space, applying a Gaussian filter to a scalar or a vector field, or letting the field evolve through a diffusion process can be interpreted as being similar operations. Indeed, the kernel of the Gaussian filter is as follows:

$$G(\mathbf{x}-\mathbf{x}') = \left(\frac{\gamma}{\pi\overline{\Delta}^2}\right)^{\frac{d}{2}} \exp\left(-\frac{\gamma|\mathbf{x}-\mathbf{x}'|^2}{\overline{\Delta}^2}\right), \tag{A1}$$

where d corresponds to the spatial dimension, $\overline{\Delta}$ is the filter width, and γ is a constant usually set to 6. The solution of the diffusion equation:

$$\partial_t \xi(\mathbf{x},t) = D\Delta\xi(\mathbf{x},t), \tag{A2}$$

where D is a diffusion coefficient and t the time, is the convolution between the scalar field $\xi(\mathbf{x}', t = 0)$, and the Green function:

$$G(\mathbf{x} - \mathbf{x}', t) = \frac{1}{(4\pi Dt)^{\frac{d}{2}}} \exp\left(-\frac{|\mathbf{x} - \mathbf{x}'|^2}{4Dt}\right) . \tag{A3}$$

So if one sets $Dt = \frac{\overline{\Delta}^2}{4\gamma}$, diffusing a scalar field through equation (A2) is equivalent to filtering that field with the convolution kernel expressed in (A1). Based on this observation, *Bülow* [2004] derived a Gaussian-like filter on the surface of a sphere of radius R, by determining the convolution kernel of the spherical diffusion equation:

$$\partial_t \xi(\mathbf{x}, t) = D\Delta_H \xi(\mathbf{x}, t) . \tag{A4}$$

which reads as follows:

$$G = \sum_{l\epsilon\mathbb{N}} \sqrt{\frac{2l+1}{4\pi}} Y_{l0} \exp\left(-\frac{l(l+1)Dt}{R^2}\right) , \tag{A5}$$

where Y_{l0} is the spherical harmonic of degree l and order $m = 0$. So in spectral space, the filtering operation of a scalar field ξ expanded in spherical harmonics:

$$\xi = \sum_{l\epsilon\mathbb{N}} \sum_{m=-l}^{m=l} \xi_{l,m} Y_{lm} \tag{A6}$$

simply reduces to the operation:

$$\overline{\xi}_{l,m} = \xi_{l,m} \exp\left(-\frac{l(l+1)\overline{\Delta}^2}{24R^2}\right) . \tag{A7}$$

Appendix B: Discretization of the Core-Mantle Boundary

B1. Construction of the Grid

The grid describing the core-mantle boundary is obtained by recursively subdividing an initial icosahedron as explained in *Baumgardner and Frederickson* [1985] and *Stuhne and Peltier* [1999]. For each grid refinement procedure, a node is added in the middle of the geodesic arc linking every two neighboring points. The refinement degree rd of the grid corresponds to the number of time this procedure has been applied. Therefore, $rd = 0$ corresponds to the icosahedron itself which possess $N_p = 12$ nodes, and $N_c = 20$ spherical triangle cells. As the refinement degree increases, the number of grid points and cells increases as follows:

$$N_p = 2 + 10 \times 4^{rd} \tag{B1}$$

$$N_c = 20 \times 4^{rd} . \tag{B2}$$

To approximate differential operators, a Voronoi-based finite volume method is chosen. This approach has been widely used in advection-diffusion problems such as in *Heikes and Randall* [1995], *Lazarov et al.* [1996], and *Satoh et al.* [2008] and has proven to be efficient to tackle these kind of problems. Since in finite volume methods, differential operators are converted to surface integrals, control volumes (or Voronoi cells) surrounding each grid points have to be defined.

As shown in Figure B1a, each grid point is surrounded by 6 (or 5 when the point corresponds to a generator of the initial icosahedron) nodes in its direct neighborhood. From this cluster of node, one can build an ensemble of spherical triangle cells $P_0P_iP_{i+1}$ all connected together by the common vertex P_0. Taking the gravity center G_i of each cell allow then to draw a hexagonal (or pentagonal) volume control around the central node P_0.

Tomita et al. [2001] and *Du et al.* [2003b] have shown that moving the grid points in a manner they coincide with the gravity center of their control volume, allow to improve the accuracy of the differential operators to the second order. The procedure employed here is the Constrained Centroidal Voronoi Tessellations

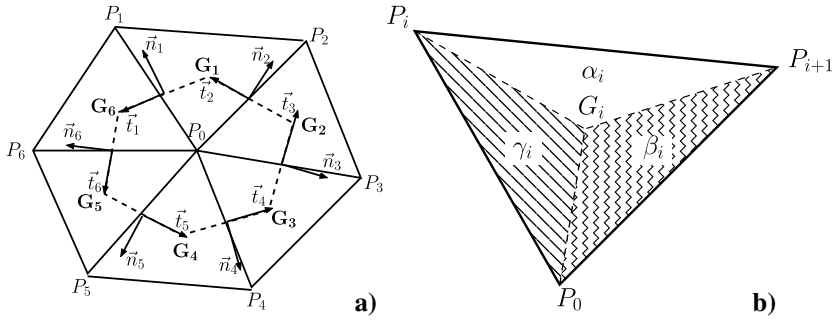

Figure B1. (a) Voronoi cell delimited by the gravity centers G_i of the different spherical triangles P_0, P_i, P_{i+1}. $\vec{n}_i$ and $\vec{t}_i$ denote, respectively, the unit vectors normal and tangential to the Voronoi cell contour. (b) Spherical triangle formed by the three nodes P_0, P_i, and P_{i+1}. G_i corresponds to the gravity center of the triangle, and α_i, β_i, and γ_i are the area of the three subtriangles.

developed by *Du et al.* [2003a]. The principle of this procedure as we implemented it, known as the Lloyd's method, is the following: (1) starting with an initial distribution of nodes on the sphere, taken here as the different subdivision of the icosahedron, as explained previously in this part; (2) building the Voronoi cells associated with each grid point; (3) moving each node to the gravity center of the cell it is belonging to; and (4) returning to Step 2 until some convergence criteria is reached. In our case, we imposed that the averaged geodesic distance between the node and the gravity center of the Voronoi cell has to be smaller than 10^{-10}.

B2. Approximation of the Differential Operators

The horizontal divergence and curl applied to a vector field $\mathbf{u}(\mathbf{x})$, and the gradient applied to a scalar field Φ can be expressed in their integral form as follows:

$$\nabla_{\mathbf{H}} \cdot \mathbf{u}(\mathbf{x}) = \lim_{\Omega \to 0} \frac{1}{\Omega} \int_{\delta_\Omega} \mathbf{u}(\mathbf{x}) \cdot \mathbf{t} \, \mathrm{d}\delta_\Omega \tag{B3}$$

$$\nabla_{\mathbf{H}} \times \mathbf{u}(\mathbf{x}) = \lim_{\Omega \to 0} \frac{1}{\Omega} \int_{\delta_\Omega} \mathbf{u}(\mathbf{x}) \cdot \mathbf{n} \, \mathrm{d}\delta_\Omega \tag{B4}$$

$$\nabla_{\mathbf{H}} \Phi = \lim_{\Omega \to 0} \frac{1}{\Omega} \int_{\delta_\Omega} \Phi \mathbf{n} \, \mathrm{d}\delta_\Omega \tag{B5}$$

where the control surface as an area Ω, delimited by the contour δ_Ω, and the unit tangential and normal vector to the contour are, respectively, $\mathbf{t}$ and $\mathbf{n}$.

On the discrete sphere, vector and scalar fields are known on the nodes; therefore, to differentiate them, one need to approximate them on the contour of the Voronoi cells. First, the different quantities are evaluated on the corners of the cells:

$$\mathbf{u}(G_i) = \frac{\alpha_i \mathbf{u}(P_0) + \beta_i \mathbf{u}(P_i) + \gamma_i \mathbf{u}(P_{i+1})}{\alpha_i + \beta_i + \gamma_i} \tag{B6}$$

$$\Phi(G_i) = \frac{\alpha_i \Phi(P_0) + \beta_i \Phi(P_i) + \gamma_i \Phi(P_{i+1})}{\alpha_i + \beta_i + \gamma_i}, \tag{B7}$$

where the areas α_i, β_i, and γ_i are shown in Figure B1b.

Then, following the notation of Figure B1a, the discrete approximation of the different differential operators becomes the following:

$$\nabla_{\mathbf{H}} \cdot \mathbf{u}(\mathbf{x}) \sim \frac{1}{A(P_0)} \sum_{i=1}^{N_G} \widetilde{G_i G}_{i+1} \frac{\left(\mathbf{u}(G_i) + \mathbf{u}(G_{i+1})\right)}{2} \cdot \mathbf{n}_i$$

$$\nabla_{\mathbf{H}} \times \mathbf{u}(\mathbf{x}) \sim \frac{1}{A(P_0)} \sum_{i=1}^{N_G} \widetilde{G_i G}_{i+1} \frac{\left(\mathbf{u}(G_i) + \mathbf{u}(G_{i+1})\right)}{2} \cdot \mathbf{t}_i$$

$$\nabla_{\mathbf{H}} \Phi \sim \sum_{i=1}^{N_G} \widetilde{G_i G}_{i+1} \frac{1}{A(P_0)} \frac{(\Phi(G_i) + \Phi(G_{i+1})}{2} \mathbf{n}_i - \frac{\Phi(P_0)}{A(P_0)} \sum_{i=1}^{N_G} \widetilde{G_i G}_{i+1} \mathbf{n}_i$$

where $A(P_0)$ corresponds to the area of the control volume, $\widetilde{G_i G}_{i+1}$ is the geodesic length between the points G_i and G_{i+1}, and N_G is the number of vertices of the control volume. Note that when the subscript $i + 1 = N_G + 1$, then $i + 1 = 1$.

Acknowledgments
The authors wish to gratefully thank Gauthier Hulot and Richard Holme for their deep review of this manuscript and the guidance they provided to improve its quality. This work has been supported by the German Research Foundation (DFG) within the Priority Program SPP1408 "Planetary Magnetism."

References

Backus, G. E. (1968), Kinematics of geomagnetic secular variation in a perfectly conducting core, *Philos. Trans. R. Soc. London, Ser. A*, *263*, 239–266, doi:10.1098/rsta.1968.0014.

Baerenzung, J., H. Politano, Y. Ponty, and A. Pouquet (2008a), Spectral modeling of turbulent flows and the role of helicity, *Phys. Rev. E*, *77*(4), 046,303, doi:10.1103/PhysRevE.77.046303.

Baerenzung, J., H. Politano, Y. Ponty, and A. Pouquet (2008b), Spectral modeling of magnetohydrodynamic turbulent flows, *Phys. Rev. E*, *78*(2), 026,310, doi:10.1103/PhysRevE.78.026310.

Baumgardner, J. R., and P. O. Frederickson (1985), Icosahedral discretization of the two-sphere, *SIAM J. Numer. Anal.*, *22*, 1107–1115, doi:10.1137/0722066.

Bayes, T. (1763), An essay towards solving a problem in the doctrine of chances, *Philos. Trans. R. Soc. London*, *53*, 370–418.

Bloxham, J. (1988), The dynamical regime of fluid flow at the core surface, *Geophys. Res. Lett.*, *15*, 585–588, doi:10.1029/GL015i006p00585.

Buffett, B. A., and U. R. Christensen (2007), Magnetic and viscous coupling at the core-mantle boundary: Inferences from observations of the Earth's nutations, *Geophys. J. Int.*, *171*, 145–152, doi:10.1111/j.1365-246X.2007.03543.x.

Bülow, T. (2004), Spherical diffusion for 3D surface smoothing, *Trans. Pattern Anal. Mach. Intell.*, *26*, 1650–1654, doi:10.1109/TPAMI.2004.129.

Chulliat, A., and G. Hulot (2000), Local computation of the geostrophic pressure at the top of the core, *Phys. Earth Planet. Inter.*, *117*, 309–328, doi:10.1016/S0031-9201(99)00104-1.

Driscoll, J. R., and D. M. Healy (1994), Computing Fourier transforms and convolutions on the 2-sphere, *Adv. Appl. Math.*, *15*(2), 202–250.

Du, Q., M. Gunzburger, and L. Ju (2003a), Constrained centroidal Voronoi tessalations for surfaces, *J. Sci. Comput.*, *24*, 1488–1506.

Du, Q., M. Gunzburger, and L. Ju (2003b), Voronoi-based finite volume methods, optimal Voronoi meshes, and PDEs on the sphere, *Comput. Meth. Appl. Mech. Eng.*, *192*, 3933–3957.

Eymin, C., and G. Hulot (2005), On core surface flows inferred from satellite magnetic data, *Phys. Earth Planet. Inter.*, *152*, 200–220, doi:10.1016/j.pepi.2005.06.009.

Fabre, Y., and G. Balarac (2011), Development of a new dynamic procedure for the Clark model of the subgrid-scale scalar flux using the concept of optimal estimator, *Phys. Fluids*, *23*(11), 115,103, doi:10.1063/1.3657090.

Finlay, C. C., and H. Amit (2011), On flow magnitude and field-flow alignment at Earth's core surface, *Geophys. J. Int.*, *186*, 175–192, doi:10.1111/j.1365-246X.2011.05032.x.

Finlay, C. C., M. Dumberry, A. Chulliat, and M. A. Pais (2010), Short timescale core dynamics: Theory and observations, *Space Sci. Rev.*, *155*, 177–218, doi:10.1007/s11214-010-9691-6.

Gamerman, D., and H. F. Lopes (2006), *Markov Chain Monte Carlo: Stochastic Simulation for Bayesian Inference*, Chapman and Hall/CRC Texts in Statistical Science Series, Taylor & Francis, Boca Raton, Fla.

Gillet, N., M. A. Pais, and D. Jault (2009), Ensemble inversion of time-dependent core flow models, *Geochem. Geophys. Geosyst.*, *10*, Q06004, doi:10.1029/2008GC002290.

Heikes, R., and D. A. Randall (1995), Numerical integration of the shallow-water equations on a twisted icosahedral grid. Part I: Basic design and results of tests, *Mon. Weather Rev.*, *123*, 1862–1880, doi:10.1175/1520-0493(1995)123<1862:NIOTSW>2.0.CO;2.

Holme, R. (2007), Large-scale flow in the core, in *Treatise on Geophysics*, edited by G. Schubert, pp. 107–130, Elsevier, Amsterdam, Netherlands, doi:10.1016/B978-044452748-6.00127-9.

Hulot, G., J. L. L. Mouël, and J. Wahr (1992), Taking into account truncation problems and geomagnetic model accuracy in assessing computed flows at the core-mantle boundary, *Geophys. J. Int.*, *108*, 224–246, doi:10.1111/j.1365-246X.1992.tb00852.x.

Hulot, G., C. Eymin, B. Langlais, M. Mandea, and N. Olsen (2002), Small-scale structure of the geodynamo inferred from Oersted and Magsat satellite data, *Nature*, *416*, 620–623.

Jackson, A. (1995), An approach to estimation problems containing uncertain parameters, *Phys. Earth Planet. Inter.*, *90*, 145–156, doi:10.1016/0031-9201(95)05080-U.

Jackson, A., J. Bloxham, and D. Gubbins (1993), Time-dependent flow at the core surface and conservation of angular momentum in the coupled core-mantle system, in *Dynamics of the Earth's Deep Interior and Earth Rotation*, vol. 72, edited by J.-L. Le Mouël, D. E. Smylie, and T. Herring, pp. 97–107, AGU Geophysical Monograph, Washington, D. C.

Lazarov, R., P. Mishev, and P. Vassilevski (1996), Finite volume method for convection-diffusion problems, *J. Numer. Anal.*, *33*, 31–55.

Leonard, A. (1974), Energy cascade in large-eddy simulations of turbulent fluid flows, in *Turbulent Diffusion in Environmental Pollution; Proceedings of the Second Symposium,* Charlottesville, Va., April 8-14, 1973, pp. 237–248, Academic Press, Inc., New York.

Lesieur, M. (2008), *Turbulence in Fluids, Fluid Mechanics and Its Applications*, Springer, Berlin, Germany.
Lesur, V., I. Wardinski, M. Hamoudi, and M. Rother (2010), The second generation of the GFZ Reference Internal Magnetic Model: GRIMM-2, *Earth, Planets, Space*, *62*, 765–773, doi:10.5047/eps.2010.07.007.
Lesur, V., I. Wardinski, and K. Whaler (2013), An attempt to build a magnetic field model under pure toroidal flow, *IAGA Scientific Assembly,* Merida, Mexico.
Mosegaard, K., and C. Rygaard-Hjalsted (1999), Probabilistic analysis of implicit inverse problems, *Inverse Prob.*, *15*, 573–583, doi:10.1088/0266-5611/15/2/015.
Pais, M. A., and D. Jault (2008), Quasi-geostrophic flows responsible for the secular variation of the Earth's magnetic field, *Geophys. J. Int.*, *173*, 421–443, doi:10.1111/j.1365-246X.2008.03741.x.
Roberts, P. H., and S. Scott (1965), On analysis of the secular variation, 1. A hydromagnetic constraint: Theory, *J. Geomagn. Geoelec.*, *17*, 137–151.
Roberts, P. H., C. Jones, and A. Calderwood (2003), Energy fluxes and Ohmic dissipation in the Earth's core, in *Earth's Core and Lower Mantle*, edited by C. A. Jones, A. M. Soward, and K. Zhang, pp. 100–129, Taylor and Francis, London.
Rygaard-Hjalsted, C., K. Mosegaard, and N. Olsen (2000), Resolution studies of fluid flow models near the core-mantle boundary using bayesian inversion, in *Methods and Applications of Inversion*, vol. 92, edited by P. Hansen, B. Jacobsen, and K. Mosegaard, pp. 255–275, Lecture Notes in Earth Sciences, Springer, Berlin Heidelberg, doi:10.1007/BFb0010296.
Sagaut, P. (2006), *Large Eddy Simulation for Incompressible Flows: An Introduction*, Scientific Computation, Springer, Berlin, Heidelberg.
Satoh, M., T. Matsuno, H. Tomita, H. Miura, T. Nasuno, and S. Iga (2008), Nonhydrostatic icosahedral atmospheric model (NICAM) for global cloud resolving simulations, *J. Comput. Phys.*, *227*, 3486–3514, doi:10.1016/j.jcp.2007.02.006.
Stuhne, G. R., and W. R. Peltier (1999), New icosahedral grid-point discretizations of the shallow water equations on the sphere, *J. Comput. Phys.*, *148*, 23–58, doi:10.1006/jcph.1998.6119.
Sukoriansky, S., B. Galperin, and N. Dikovskaya (2002), Universal spectrum of two-dimensional turbulence on a rotating sphere and some basic features of atmospheric circulation on giant planets, *Phys. Rev. Lett.*, *89*(12), 124501, doi:10.1103/PhysRevLett.89.124501.
Sun, O. S., and L. K. Su (2007), Resolution and Reynolds number effects on LES of turbulent round jet mixing, *60th Annual Meeting, American Physical Society Division of Fluid Dynamics,* Salt Lake City, Utah.
Thebault, E., and F. Vervelidou (2013), A theoretical spherical spatial power spectrum of the Earths lithospheric magnetic field, in *EGU General Assembly Conference Abstracts*, vol. 15, p. 5250.
Tomita, H., M. Tsugawa, M. Satoh, and K. Goto (2001), Shallow water model on a modified icosahedral geodesic grid by using spring dynamics, *J. Comput. Phys.*, *174*, 579–613, doi:10.1006/jcph.2001.6897.
Velímský, J. (2010), Electrical conductivity in the lower mantle: Constraints from CHAMP satellite data by time-domain EM induction modelling, *Phys. Earth Planet. Inter.*, *180*, 111–117, doi:10.1016/j.pepi.2010.02.007.
Voorhies, C. V. (2004), Narrow scale flow and a weak field by the top of Earth's core: Evidence from Orsted, Magsat and secular variation, *109*, B03106, doi:10.1029/2003JB002833.